Predicting Ice Shape Evolution in a Bulk Microphysics Model

ANDERS A. JENSEN

National Center for Atmospheric Research, Boulder, Colorado

JERRY Y. HARRINGTON

The Pennsylvania State University, University Park, Pennsylvania

HUGH MORRISON

National Center for Atmospheric Research, Boulder, Colorado

JASON A. MILBRANDT

Meteorological Research Division, Environment and Climate Change Canada, Montreal, Quebec, Canada

(Manuscript received 2 December 2016, in final form 21 February 2017)

ABSTRACT

A novel bulk microphysics scheme that predicts the evolution of ice properties, including aspect ratio (shape), mass, number, size, and density is described, tested, and demonstrated. The scheme is named the Ice-Spheroids Habit Model with Aspect-Ratio Evolution (ISHMAEL). Ice is modeled as spheroids and is nucleated as one of two species depending on nucleation temperature. Microphysical process rates determine how shape and other ice properties evolve. A third aggregate species is also employed, diversifying ice properties in the model. Tests of ice shape evolution during vapor growth and riming are verified against wind tunnel data, revealing that the model captures habit-dependent riming and its effect on fall speed. Lagrangian parcel studies demonstrate that the bulk model captures ice property evolution during riming and melting compared with a bin model. Finally, the capabilities of ISHMAEL are shown in a 2D kinematic framework with a simple updraft. A direct result of predicting ice shape evolution is that various states of ice from unrimed to lightly rimed to densely rimed can be modeled without converting ice mass between predefined ice categories (e.g., snow and graupel). This leads to a different spatial precipitation distribution compared with the traditional method of separating snow and graupel and converting between the two categories, because ice in ISHMAEL sorts in physical space based on the amount of rime, which controls the thickness and therefore fall speed. Predicting these various states of rimed ice leads to a reduction in vapor growth rate and an increase in riming rate in a simple updraft compared with the traditional approach.

1. Introduction

The complex shapes, various sizes, and liminal nature of ice particles in the atmosphere make it difficult to model microphysical growth processes accurately. Growth equations depend on ice properties like particle shape (habit) and size. Habits develop by preferential vapor-depositional growth along one axis altering the cross-sectional area, fall speed, and collection kernel for liquid drops (riming) and ice (aggregation) (Mason 1953; Hallett 1965; Ono 1970; Takahashi and Fukuta 1988; Takahashi et al. 1991; Fukuta and Takahashi 1999). To complicate the matter, ice habit diagrams (e.g., Magono and Lee 1966; Bailey and Hallett 2009) show that ice shape can change substantially over a few degrees Celsius. Unsurprisingly, cold cloud systems are considerably sensitive to the evolution of ice properties: for example, mixed-phase cloud lifetime (Avramov and Harrington 2010; Sulia et al. 2014), the distribution of orographically enhanced precipitation (Colle et al. 2005; Garvert et al. 2005; Woods et al. 2007), and the structure and evolution of mesoscale convective systems (Fovell and Ogura 1988; Szeto and Cho 1994; Adams-Selin et al. 2013; Morrison et al. 2015).

Microphysics schemes cannot account for all of the observed variability in atmospheric ice properties. In

Corresponding author: Anders A. Jensen, ajensen@ucar.edu

DOI: 10.1175/JAS-D-16-0350.1

traditional schemes it is assumed that ice can be represented by a few predefined categories, such as cloud ice, snow, and graupel. For each category, ice mass and terminal fall speed are related to a maximum diameter using different mass–dimensional (m–D) and fall speed–dimensional (v_t–D) relationships. These relationships allow, for example, modeled graupel to be compact and fast falling and modeled snow (for the same mass) to be less compact and slower falling. Complex particle shapes and vastly different fall speeds can be intrinsically represented using m–D and v_t–D relationships, but those shapes and fall speeds are assumed a priori. While effective in distinguishing properties of snow from graupel, using m–D relationships means that all snow particles have the same mass for a given diameter. Thus, all modeled snowflakes evolve along the same trajectory in mass–size space.

A problem with separating snow and graupel into different categories is that rimed snow is converted to graupel, but this conversion process is inherently artificial. In nature, as snow particles rime, their physical properties continuously evolve from those of unrimed snow, to snow with an increasing degree of riming, and eventually to graupel. In traditional schemes, some rimed snow mass converts to graupel, while the rest remains as snow because these schemes cannot model the transitional rimed states of ice. While mass is conserved between categories, other particle properties, such as fall speed and maximum dimension, may evolve unnaturally. Furthermore, the amount of rimed snow converted to graupel is typically determined by ad hoc or tunable parameters that cannot be directly measured. Studies have shown sensitivity to these conversion parameters, and this can bias model output systematically (Morrison and Grabowski 2008; Lin and Colle 2009).

Partially rimed ice can be included in the traditional approach by adding more ice categories (e.g., Straka and Mansell 2005). However, m–D and v_t–D relationships for partially rimed ice do not capture the appropriate transitions in ice particle mass and fall speed that occur during riming (Jensen and Harrington 2015). Observations and theory show that, as particles rime, the supercooled cloud droplets freeze primarily along the minor axis length (Heymsfield 1982; Takahashi and Fukuta 1988; Fukuta and Takahashi 1999). Light riming either thickens (extends the minor axis) or fills in gaps (increases the effective density) of the ice particles, which leads to a fall speed increase with no increase in the maximum dimension; this process is in contrast to m–D relationships for rimed ice, which relate mass and fall speed increases to maximum dimension increases. The minor axis grows until the particle becomes quasi spherical, at which point it tumbles as it falls and remains quasi spherical.

Newer modeling approaches have attempted to remove the abrupt, artificial transitions between predefined ice categories. For instance, Thompson et al. (2008) and Lin and Colle (2011) attempt to improve the fall speed increase during riming. Erfani and Mitchell (2017) used measurements and theory to constrain rime-mass growth while fixing maximum dimension such that the method can be used with m–D relationships in a more physically consistent way. ''Particle property'' methods have also been developed where ice properties are explicitly predicted rather than assumed with predefined categories (Chen and Lamb 1994, 1999; Hashino and Tripoli 2007; Morrison and Grabowski 2008; Harrington et al. 2013a; Chen and Tsai 2016). Morrison and Grabowski (2008) allowed rime-mass fraction to evolve in space and time such that partially rimed ice was explicitly represented. Their method ties together m–D relationships for snow and graupel, allowing smooth transitions in m–D parameter space as rime-mass fraction changes. Tests reveal significant changes in precipitation rate when the snow–graupel threshold is removed (Morrison and Grabowski 2008). More recently, Morrison and Milbrandt (2015) developed a bulk scheme [Predicted Particle Properties (P3)] that predicts both the rime mass and rime volume, with predicted rime density (Milbrandt and Morrison 2013), in addition to mass and number. P3 improves the distribution of surface precipitation for both a simulated squall line and an orographic precipitation case compared with many traditional schemes (Morrison et al. 2015).

While the P3 scheme accounts for transitional rimed states of ice as well as changes in rime density, ice particle growth by vapor deposition in P3 is constrained by m–D relationships that are chosen a priori. Wind tunnel data (Takahashi and Fukuta 1988; Takahashi et al. 1991; Fukuta and Takahashi 1999) and simulations (Wang and Ji 2000; Jensen and Harrington 2015) reveal that size and shape variations among ice particles substantially impact how they rime. Isometric ice particles more readily rime as a result of larger collision efficiencies and fall speeds than ice particles with more eccentric (less spherical) shapes. At low enough liquid water contents, isometric habits can collect rime, whereas dendrites, for instance, cannot. Modeling this habit-dependent riming without using predefined categories requires the prediction of ice particle shape. Chen and Lamb (1994) developed a model that predicts two ice particle axis lengths, and thus shape, during vapor growth. This adaptive-habit (AHAB) approach couples mass growth to temperature-dependent ice particle shape evolution. Shape evolution feeds into the vapor growth equation,

producing various habits with different masses, shapes, maximum dimensions, densities, and fall speeds. Because ice shape evolves smoothly, the conversion from cloud ice to snow used in traditional schemes (Ferrier 1994; Harrington et al. 1995) is not needed.

The Chen and Lamb (1994) approach can be extended to parameterize shape changes during riming. Jensen and Harrington (2015) developed a theoretical single-ice-particle model that evolves mass, shape, maximum dimension, density, and fall speed during both vapor growth and riming. The shape-dependent evolution of mass and fall speed from this model agrees well with wind tunnel data of riming nonspherical ice observed between −3° and −18°C; for instance, isometric ice grown near −10°C rimes earlier and faster than dendrites grown near −15°C or columns grown near −6°C. Moreover, the model produces a range of rimed states (e.g., from lightly to heavily rimed dendrites) depending on the growth time, ice particle size, and the cloud-droplet size spectrum (Jensen and Harrington 2015). This spread in particle properties due to riming is evident from observations (Locatelli and Hobbs 1974) but cannot be captured by traditional m–D relationships. Representing these different rimed states using the traditional approach would require adding a multitude of categories to represent a veritable continuum of particle types (e.g., from lightly rimed dendrites to moderately rimed ice to graupel) which is not practical; moreover, such an approach would still require mass conversion between these categories.

Here we extend the bulk framework of Harrington et al. (2013a), which predicts particle evolution from vapor deposition and sublimation, so that it predicts the evolution of ice particle properties (mass, aspect ratio, maximum dimension, density, and fall speed) as a result of all relevant microphysical processes: nucleation, vapor deposition, sublimation, riming, melting, and aggregation. In this paper, we describe the new bulk scheme, compare the bulk shape–evolving riming parameterization to observations and a detailed particle-tracking bin microphysics model, and compare the new scheme to a traditional m–D scheme within a simplified kinematic modeling framework.

2. The adaptive-habit framework: Single-ice-particle shape evolution

The bulk microphysics scheme is rooted in the AHAB single-ice-particle shape evolution theory for vapor growth (Chen and Lamb 1994). This theory has been used to model particle shape evolution during vapor growth and riming, with wind tunnel data used for corroboration (Jensen and Harrington 2015). In this section, the theory is explained and generalized because it is used for vapor growth, riming, and melting. The single-particle equations will be extended to a bulk distribution in the next section.

The AHAB approach uses two spatial dimensions to characterize the shape of growing ice particles. While these dimensions are rooted in the six-fold symmetry of ice that is characterized by the crystallographic a and c axes, one can also think of the parameterization method as predicting the evolution of a major and minor dimension of the ice particles. This is the main reason why spheroids are used to characterize the shape of modeled ice instead of hexagonal prisms: only a subset of atmospheric ice is hexagonal prisms, whereas the vast majority of atmospheric ice has more complex shapes (i.e., dendrites, hollow columns, and rosettes, to name a few). Using spheroids as an approximation for atmospheric ice particle shapes makes the parameterization applicable to a broader range of ice particles, as long as a quantitative method to distribute the mass and density gained during growth along both the a-axis length a_i and c-axis length c_i is used. The shape, or aspect ratio ϕ_i, of modeled ice is defined as

$$\phi_i \equiv \frac{c_i}{a_i}. \tag{1}$$

Modeled ice can be oblate (e.g., planar ice) when $a_i > c_i$ ($\phi_i < 1$) or prolate (e.g., columnar ice) when $c_i > a_i$ ($\phi_i > 1$).

For spheroidal ice, the mass m_i, axis lengths, and effective particle density ρ_i (here called particle density) are related by

$$m_i = \rho_i \frac{4}{3} \pi a_i^2 c_i. \tag{2}$$

Particle densities are generally used in numerical modeling as an approximation of complex particle types. For instance, a graupel density of 400 kg m^{-3} is often used to represent the porous nature of rimed ice, whereas a snow density of 100 kg m^{-3} is used to represent dendritic branches (cf. Ferrier 1994).

Considering the evolution of a single ice particle, mass tendencies are calculated for different microphysical processes (e.g., vapor growth, riming, and melting), and all have equations for mass evolution of the form

$$\left.\frac{dm_i}{dt}\right|_x = \rho_x \left.\frac{dV_i}{dt}\right|_x, \tag{3}$$

where x is the process, V_i is the ice particle volume, and ρ_x is the growth density. Note that ρ_x is a density of the

mass added during growth for process x, while ρ_i is the particle density. Chen and Lamb (1994) describe the development of secondary habits using a deposition density $\rho_x = \rho_{\text{dep}}$ that is a function of temperature T and supersaturation, and Macklin (1962) parameterize the development of porous ice during riming by a rime density $\rho_x = \rho_{\text{rime}}$ that is a function of temperature, cloud-droplet size, and collisional impact velocity. Microphysical process-rate parameterizations for mass evolution are described in section 3e.

Mass evolution alone is insufficient to model the evolution of the particle dimensions, since m_i depends on both a_i and c_i [Eq. (2)]. In order to link the mass evolution to the axis growth rates, Chen and Lamb (1994) provided a mass-distribution hypothesis that relates changes in a_i to c_i during vapor growth, where

$$\left.\frac{dc_i}{da_i}\right|_{\text{dep}} = \delta_{\text{dep}}(T)\phi_i. \tag{4}$$

The inherent growth ratio for vapor deposition δ_{dep}, derived from laboratory measurements (Lamb and Scott 1972), is the ratio of how efficiently water molecules incorporate along the c and a axes. Ice shape is controlled by δ_{dep} with $\delta_{\text{dep}} = 1$, causing ϕ_i to be constant and $\delta_{\text{dep}} < 1$ ($\delta_{\text{dep}} > 1$) leading to the development of oblate (prolate) shapes.

Other microphysical growth processes also cause the shapes of individual ice particles to evolve, and, thus, a general mass-distribution hypothesis must be formulated. Riming and melting are treated with separate mass-distribution hypotheses (δ_{rime} and δ_{melt}), whereas aggregation is not parameterized with a value of δ_x because aggregation is not relevant for single-particle growth; aggregation will be discussed in section 3e(5). Axis-length changes from each single-ice-particle axis-length-evolution (SIP-ALE) process (vapor growth, sublimation, riming, and melting) are calculated generally using δ_x.

Equation (4) provides a quantitative link between the a and c dimensions of the ice particle and can be tied to the mass evolution. Combining the logarithmic derivatives of ϕ_i and V_i and using Eq. (4), Chen and Lamb (1994) showed that changes in ice particle volume are related to changes in aspect ratio by

$$\frac{d\phi_i}{\phi_i} = \left(\frac{\delta_x - 1}{\delta_x + 2}\right)\frac{dV_i}{V_i}. \tag{5}$$

This equation has been tested against laboratory-grown ice and was shown to be accurate for both vapor growth (Chen and Lamb 1994; Sulia and Harrington 2011; Harrington et al. 2013b) and riming (Jensen and Harrington 2015).

One of the benefits of the AHAB approach is that the method is rooted in "fundamental" parameters like δ_{dep} that can be determined from laboratory measurements (Lamb and Scott 1972; Libbrecht 2003) or δ_{rime} that can be empirically determined from wind tunnel measurement (Jensen and Harrington 2015). Measurements from Lamb and Scott (1972) provide values of δ_{dep} for only single crystalline ice, but values of δ_{dep} for bullet rosettes (see Sheridan 2008) and planar ice at temperatures less than −20°C (Hashino and Tripoli 2007) have also been determined.

3. ISHMAEL: A complete bulk AHAB model

The single-particle model discussed in the previous section provides the framework for the bulk adaptive-habit ice parameterization. The complete bulk microphysics model employing the AHAB framework is named the Ice-Spheroid Habit Model with Aspect-Ratio Evolution (ISHMAEL) and is described in this section. ISHMAEL builds off of previous work on the single ice species bulk adaptive-habit vapor-growth model (Harrington et al. 2013a,b; Sulia et al. 2013).

a. Conservation equation for prognostic scalars

Each hydrometeor species in ISHMAEL is represented by one or more conserved, prognostic scalar χ, governed by

$$\frac{\partial \chi}{\partial t} = -\mathbf{u}\cdot\nabla\chi + \frac{1}{\rho_a}\frac{\partial(\rho_a V_\chi \chi)}{\partial z} + S_\chi, \tag{6}$$

where t is time, z is height, ρ_a is the air density, $\mathbf{u}$ is the 3D wind vector, V_χ is the appropriately weighted fall speed of χ, and S_χ represents source and sink terms.

b. Liquid prognostic variables and process rates

The liquid prognostic variables in ISHMAEL are cloud water q_C, and rainwater q_R mass mixing ratios, as well as rainwater number mixing ratio n_R. Cloud number concentration is assumed constant ($N_C = 200\,\text{cm}^{-3}$). The raindrop size distribution is assumed to follow an inverse-exponential distribution (Marshall and Palmer 1948) and to calculate riming rates the cloud-droplet size distribution is assumed to be a lognormal distribution (see, e.g., Frisch et al. 2002). Warm rain processes are parameterized as follows. Conversion of cloud water to rain and accretion of cloud water by rain are parameterized following Khairoutdinov and Kogan (2000). Self-collection of rain comes from Beheng (1994),

raindrop breakup comes from Verlinde and Cotton (1993), and evaporation of rain follows Rutledge and Hobbs (1983).

c. Ice prognostic variables

The number of ice hydrometer species used in ISHMAEL is flexible. However, if only one ice species is used, the properties of that ice species will be weighted towards those of the largest mass sources (Milbrandt and Morrison 2016). For example, this could cause small columns, if mixed with large dendrites (either explicitly through parameterized mixing or implicitly through advection), to be "lost" after the properties of the columns and dendrites are mixed. To obviate this issue, ice is nucleated as oblate (prolate) when $\delta_{\rm dep}(T) \le 1$ [$\delta_{\rm dep}(T) > 1$], allowing two different habits to exist in the same grid cell. Note that, even though nucleation into a given species depends on the inherent growth ratio, the properties of both ice species evolve freely and can even change habit type (i.e., change from oblate to prolate or vice versa depending on growth processes). Therefore, these ice species will be referred to as ice one and ice two. Similarly, in the interest of preserving ice properties, aggregates are parameterized as a separate ice species because aggregation can drastically change ice shape, size, and density. Hence, the hydrometeor species in ISHMAEL are cloud water, rainwater, and three ice species.

Along with the traditional two-moment variables, mass q_I, and number n_I mixing ratios, two volume-dimensioned mixing ratios ϑ_I and ψ_I, related to the a and c axes, are prognosed [Eqs. (11) and (12)] for each ice species. Two volume-dimensioned mixing ratios are used to advect the two axis lengths while preserving density. The bulk prognostic formulations are general for all ice species and will therefore be written with the subscript "I." When discussing a specific ice species, the notation will be q_1, q_2 (for ice one and ice two, respectively), and q_3 (aggregates). Ice properties, such as aspect ratio and density, will be used to classify these ice species diagnostically, for example, as dendrites or low-density graupel. A schematic of the ice species is shown in Fig. 1. Table 1 provides a list of bulk model variables.

As in many schemes, the ice particle size distribution follows a gamma function, expressed as a function of the a-axis length a_i (Harrington et al. 2013a) such that

$$n(a_i) = \frac{N_I}{\Gamma(\nu)} \left(\frac{a_i}{a_n}\right)^{\nu-1} \frac{1}{a_n} \exp\left(-\frac{a_i}{a_n}\right), \tag{7}$$

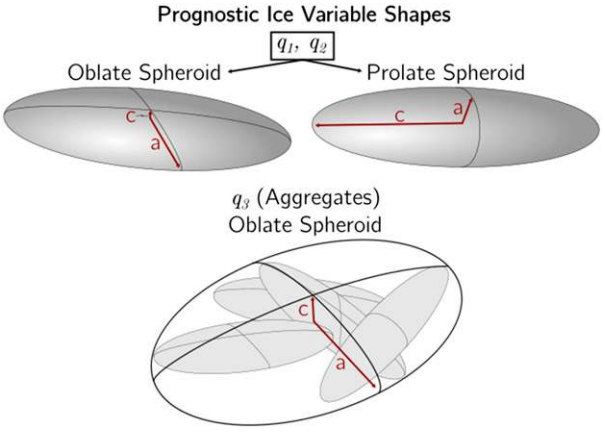

FIG. 1. A schematic of the ice species used in ISHMAEL. When $\delta_{\rm dep} \le 1 (\delta_{\rm dep} > 1)$ ice nucleates as q_1 (q_2). These two species can evolve to be oblate or prolate spheroids. Note that aggregates are assumed to be oblate spheroids.

where N_I is the total ice number concentration ($n_I = N_I/\rho_a$), Γ is the gamma function, ν is the distribution shape parameter, and a_n is the characteristic a-axis semilength. The key to using a single size spectrum [Eq. (7)] in a model that predicts two axis lengths is to derive an equation relating the two axes from Eq. (4). Harrington et al. (2013a) showed that, for a single ice particle, a_i and c_i are related by

$$c_i = a_0^{1-\delta_*} a_i^{\delta_*}, \tag{8}$$

where a_0 is the initial (nucleation) size, and the power-law exponent δ_* [see Harrington et al. (2013a), their Eq. (6)] is an average of the various δ_x that drive particle shape evolution, and it therefore changes in time; the various δ_x are used to change particle shape through Eq. (5), and δ_* is diagnosed at any time from a_i and c_i. All particles are nucleated as isometric ice ($\delta_* = 1$) and evolve into oblate ice ($\delta_* < 1$) or prolate ice ($\delta_* > 1$) or remain isometric. Using Eq. (8), the mass mixing ratio can be written in terms of the a-axis length alone:

$$\begin{aligned} q_I &= \frac{1}{\rho_a} \int_0^\infty m_i(a_i, c_i) n(a_i)\, da_i \\ &= \rho_I \underbrace{\frac{N_I}{\rho_a} [(4/3)\pi a_0^{1-\delta_*} a_n^{2+\delta_*}] \frac{\Gamma(\nu + 2 + \delta_*)}{\Gamma(\nu)}}_{V_I}, \end{aligned} \tag{9}$$

where ρ_I is a volume-weighted effective density, V_I is the total volume mixing ratio, and the term in square brackets is the single-particle volume at size a_n. Note that ρ_I is a total mass mixing ratio divided by a total

TABLE 1. ISHMAEL model variables.

Variable (unit)	Description
t (s)	Time
Δt (s)	Model time step
T (K)	Temperature
ρ_a (kg m^{-3})	Air density
q_I (kg kg^{-1})	Ice mass mixing ratio
n_I (kg^{-1})	Ice number mixing ratio
ϑ_I (m^3 kg^{-1})	Ice volume mixing ratio
ψ_I (m^3 kg^{-1})	Ice volume × aspect ratio mixing ratio
q_V(kg kg^{-1})	Water vapor mixing ratio
q_C (kg kg^{-1})	Cloud water mass mixing ratio
q_R (kg kg^{-1})	Rainwater mass mixing ratio
n_R (kg^{-1})	Rainwater number mixing ratio
N_I (m^{-3})	Ice number concentration
Γ	Gamma function
ν	Ice distribution shape parameter
a_n (m)	Ice distribution characteristic a-axis length
c_n (m)	Ice distribution characteristic c-axis length
r_n (m)	Ice distribution characteristic r-axis length
V_I (m^3 kg^{-1})	Total ice distribution volume mixing ratio
ρ_I (kg m^{-3})	Ice distribution volume-weighted density
ρ_b (=920 kg m^{-3})	Bulk density of ice
ρ_x (kg m^{-3})	Growth density for process x
a_0 (=0.1 μm)	Initial ice size
δ_x	Ratio of the axis growth efficiencies for process x
δ_*	Integrated growth history parameter
ϕ_I	Ice number–weighted aspect ratio
a_I (m)	Ice mass–weighted a-axis length
c_I (m)	Ice mass–weighted c-axis length
D_I (m)	Ice mass–weighted maximum diameter
v_{t_I} (m s^{-1})	Ice mass–weighted fall speed

spheroidal volume mixing ratio, and therefore ρ_I can remain larger than densities calculated in traditional models that use an equivalent volume sphere. Writing mass in terms of one axis only is beneficial because mass is then related to size in a similar way as using m–D relationships (Harrington et al. 2013a) except that the coefficients evolve in time and space.

Changing variables in Eq. (7) using Eq. (8) allows the size distribution to be written in terms of the characteristic c-axis length c_n or the characteristic equivalent-volume spherical radius r_n, where $r_n^3 = a_n^2 c_n$ (Harrington et al. 2013a). Integrating both the axis relationship [Eq. (8)] and the mass-distribution hypothesis [Eq. (4)] over the size distribution [Eq. (7)] gives relationships between the characteristic sizes (Harrington et al. 2013a):

$$\frac{dc_n}{da_n} = \delta_x \frac{c_n}{a_n} \tag{10a}$$

and

$$c_n = a_0^{1-\delta_*} a_n^{\delta_*}. \tag{10b}$$

Equations (10a) and (10b) are the distribution counterparts to the single-particle equations [Eqs. (4) and (8)].

Adding shape evolution means time tendencies for each axis length must be computed, and two measures of mean particle size (functions of a_n and c_n) must be advected. When choosing prognostic variables for axis-length advection, two conditions must be met. First, δ_* should be preserved during advection when initially constant, since the aspect ratio in this instance should not change by transport alone. Second, density needs to be preserved during advection as well; ρ_I is a key variable that accounts for secondary habits and changes in density during riming, impacting fall speeds. Density is preserved without attendant errors in size if it is proportional to the ratio of two advected variables with the same advective Courant number (Morrison et al. 2016). Density is proportional to q_I/V_I, and because V_I ($\propto a_n^2 c_n$) advects with the same velocity as mass, it is logical to advect a measure of bulk volume,

$$\vartheta_I = \frac{N_I}{\rho_a} a_n^2 c_n. \tag{11}$$

Sulia et al. (2013) showed that δ_* is preserved during advection provided the ratio of the advected size variables is the bulk characteristic aspect ratio ($\phi_n \equiv c_n/a_n$); hence, we also prognose $a_n^2 c_n \phi_n$, or

$$\psi_I = \frac{N_I}{\rho_a} a_n c_n^2. \tag{12}$$

d. Updating ice prognostic variables

In this section we describe the method used to evolve the prognostic variables that account for mass, number, shape, and density in ISHMAEL. The initial values of the prognostic ice variables before a microphysics time step Δt are $q_I(t)$, $n_I(t)$, $\vartheta_I(t)$, and $\psi_I(t)$. From these variables, $a_n(t)$ and $c_n(t)$ are calculated [from Eqs. (11) and (12)], and $\delta_*(t)$ is diagnosed [from Eq. (10b)].

The procedure to update prognostic variables depends on the process rate and, for now, the ice species. Shape evolution is currently not parameterized for aggregates (q_3), and therefore, the following discussion of prognostic variable evolution only applies to ice one and ice two. The subsections below are divided into two parts: First, we describe the general procedure for evolving mass, axis length, and density due to any process rate and nucleation. Second, we describe the individual bulk process rates (section 3e).

1) GENERAL MASS-TENDENCY EQUATION

Integrating the single-particle mass tendency equation [Eq. (3)] for an arbitrary microphysical process over the size spectrum gives the mass mixing ratio tendency

$$\frac{dq_I}{dt}_x = \rho_x \frac{dV_I}{dt}_x . \tag{13}$$

The growth density ρ_x changes the volume-weighted density by

$$\rho_I(t+\Delta t) = (1-w_x)\rho_I(t) + w_x\rho_x , \tag{14}$$

where

$$w_x = \frac{(dq_I/dt)_x}{q_I(t)}\Delta t . \tag{15}$$

The weighting function w_x appropriately weights the growth density by the fractional change in mass due to a given process.

2) PROGNOSTIC VARIABLE EVOLUTION DURING SIP-ALE PROCESSES

Updating particle shape during SIP-ALE processes follows from Harrington et al. (2013a). This requires calculating the bulk volume mixing ratio tendency [cf. Eq. (5)]. To evolve bulk shape, a_n is updated by integrating Eq. (10b) over a model time step and replacing the fractional change in c_n with the fractional change in V_I, where

$$a_n(t+\Delta t) = a_n(t)\left[\frac{V_I(t+\Delta t)}{V_I(t)}\right]^{1/(2+\delta_x)} . \tag{16}$$

Note that δ_* is assumed constant during the time step for the growth calculations, which is reasonable provided $\Delta t < 20$ s (Harrington et al. 2013a). To update δ_* for the time step, r_n is first updated from $V_I(t+\Delta t)$. Taking the natural logarithm of Eq. (10a) and replacing c_n with r_n yields

$$\delta_*(t+\Delta t) = \frac{3\ln[r_n(t+\Delta t)] - 2\ln[a_n(t+\Delta t)] - \ln a_0}{\ln[a_n(t+\Delta t)] - \ln a_0} . \tag{17}$$

After updating a_n, the number-weighted aspect ratio is updated as

$$\frac{\phi_I(t+\Delta t)}{\phi_I(t)} \approx \left[\frac{V_I(t+\Delta t)}{V_I(t)}\right]^{(\delta_x-1)/(\delta_x+2)} \quad \text{where}$$
$$\phi_I = \frac{c_n}{a_n}\frac{\Gamma(\nu+\delta_*-1)}{\Gamma(\nu)}, \tag{18}$$

the approximation coming from assuming a constant value of δ_* (Harrington et al. 2013a). Finally, c_n is updated from ϕ_I and a_n (Harrington et al. 2013a):

$$c_n(t+\Delta t) = \begin{cases} \phi_I(t+\Delta t)a_n(t+\Delta t)\dfrac{\Gamma(\nu)}{\Gamma(\nu+\delta_*-1)}, & \text{if} \quad \delta_* \le 1 \\ a_0^{1-\delta_*(t+\Delta t)}a_n(t+\Delta t)^{\delta_*(t+\Delta t)}, & \text{if} \quad \delta_* > 1 . \end{cases} \tag{19}$$

3) PROGNOSTIC VARIABLE EVOLUTION FOR PROCESSES AFFECTING NUMBER CONCENTRATION

The number mixing ratio is held constant during the aspect ratio and density changes described above. Particles that completely sublimate or melt (along with aggregation and nucleation) constitute a loss of number concentration $(dN_I/dt)_x$ and mass. For sublimation and melting, number loss is assumed to occur with constant δ_* since the parcel simulations of Harrington et al. (2013b) show that this assumption is reasonable. Therefore, the same approximation (constant δ_*) is made when mass and number loss occur (for ice one and ice two) during aggregation.

During ice nucleation and freezing of rain, large changes in bulk average shape can occur as a result of the addition of potentially large, spherical ice to the distribution. This implies that changes in δ_* from these processes should be considered. Updating δ_* after nucleation and freezing of rain requires determining how these two processes affect both a_n and c_n. The mass-weighted distribution sizes and the mass-weighted nucleation size are used to update δ_*. The mass-weighted axis lengths are

$$a_I(t) = a_n(t)\frac{\Gamma[\nu+3+\delta_*(t)]}{\Gamma[\nu+2+\delta_*(t)]} \quad \text{and}$$
$$c_I(t) = c_n(t)\frac{\Gamma[\nu+2+2\delta_*(t)]}{\Gamma[\nu+2+\delta_*(t)]}, \tag{20}$$

and the mass-weighted nucleation size r_{nuc} can be determined from $(dq_I/dt)_{\text{nuc}}$, $(dN_I/dt)_{\text{nuc}}$, and ρ_{nuc}, assuming

nucleated ice is spherical. Updating the mass-weighted sizes from nucleation yields

$$a_I(t+\Delta t) = (1-w_{\text{nuc}})a_I(t) + w_{\text{nuc}}r_{\text{nuc}} \quad \text{and}$$
$$c_I(t+\Delta t) = (1-w_{\text{nuc}})c_I(t) + w_{\text{nuc}}r_{\text{nuc}}, \tag{21}$$

and these are used to calculate $\delta_*(t+\Delta t)$.

For all microphysical processes involving a change in number concentration, values of $q_I(t+\Delta t)$, $n_I(t+\Delta t)$, $\rho_I(t+\Delta t)$, and $\delta_*(t+\Delta t)$, as described above, are used to diagnose $a_n(t+\Delta t)$ and $c_n(t+\Delta t)$.

4) Prognostic variable evolution for aggregates

Aggregates are currently treated as a traditional ice category: mass and number mixing ratio tendencies are predicted, and the maximum diameter is diagnosed assuming constant shape and density ($\phi_3 = 0.2$ and $\rho_3 = 50\,\text{kg}\,\text{m}^{-3}$), which allows both ϑ_3 and ψ_3 to be diagnosed. The volume-weighed density is chosen based on data from Locatelli and Hobbs (1974). Vapor growth, riming, and melting evolve the mass and maximum dimension of aggregates but not the density and shape. Future work will improve this aggregation parameterization by including both shape and density evolution for aggregates.

e. Ice microphysical process rates

The evolution of mass, number, aspect ratio, size, and density described above requires the individual mass and number mixing ratio process rates [Eq. (13)], values of ρ_x, and values of δ_x (if applicable).

1) Vapor-depositional growth and sublimation

The change in mass mixing ratio because of deposition and sublimation is

$$\left(\frac{dq_I}{dt}\right)_{\text{dep}} = \frac{1}{\rho_a}\int_0^\infty 4\pi C_i G_i s_i n(a_i)\,da_i = \frac{N_I}{\rho_a}4\pi C_I G_i s_i, \tag{22}$$

where C_I is the distribution-averaged capacitance [Harrington et al. 2013a, their Eq. (B14)], G_i is an effective diffusion coefficient that accounts for vapor diffusion, thermal conduction, and ventilation,[1] and s_i is the ice supersaturation. Equation (22) is solved explicitly for $r_n(t+\Delta t)$ following Harrington et al. (2013a). Calculation of ρ_{dep} comes from Jensen and Harrington (2015).

Number loss during sublimation is assumed to be proportional to w_{sub} (Ferrier 1994), where

$$\left(\frac{dN_I}{dt}\right)_{\text{sub}} = \frac{w_{\text{sub}}}{\Delta t}N_I, \tag{23}$$

though there are errors in making this approximation that depend on ice shape and ν (cf. Harrington et al. 1995). Note that w_{sub} can be calculated using Eq. (15).

2) Riming

To calculate bulk riming rates, the numerical approach of Jensen and Harrington (2015) is used because the collision efficiencies cannot be integrated analytically. The ice and rain size distributions (both assumed to be gamma distributions) are normalized and binned linearly in equivalent-volume radius space over a size range from 0.05 to 40 times the characteristic radii using 200 bins. Cloud water bins (also 200) are log spaced, from 0.1 to 20 times the median radius, which is related to the liquid water content [see, e.g., Miles et al. (2000), their Eq. (7d)], to capture the variation at small sizes. Rain is collected as rime only when the binned-ice fall speed is larger than the binned-rain fall speed. Otherwise, rain is nucleated as frozen drops [see section 3e(4)].

The riming rate for a single-ice-particle collecting a distribution of liquid drops (dm_r/dt) follows Jensen and Harrington (2015). Applying the collection equation to a binned distribution of ice to calculate the total bulk riming rate yields

$$\left(\frac{dq_I}{dt}\right)_{\text{rime}} = \frac{1}{\rho_a}\sum_i \left.\frac{dm_r}{dt}\right|_i N_i$$
$$= \frac{1}{\rho_a}\sum_i \left(\sum_\ell E_{i\ell}A_g\,|\,v_i - v_\ell\,|\,m_\ell n_\ell\right)_i N_i, \tag{24}$$

where $E_{i\ell}$ is the collision efficiency, A_g is the geometrical cross-sectional area for collision, v_i is the ice-particle fall speed, v_ℓ is the liquid-drop fall speed, m_ℓ is the mass of liquid, n_ℓ is the number concentration of liquid drops, and N_i is the number concentration of ice particles in bin i. Calculation of $E_{i\ell}$ follows the explicit method of Jensen and Harrington (2015) that is able to produce collision efficiencies for both oblate and prolate spheroids. Terms in Eq. (24) depend on ice properties: A_g depends on the ice cross-sectional area and v_i is a function of ice shape, density, and maximum dimension.

Rime density varies with ice, liquid, and environmental properties: Higher temperature, higher impact velocity, and larger drop size all lead to larger values of rime density. To parameterize an average value of rime density $\overline{\rho}_{\text{rime}}$, data from Macklin (1962, their Fig. 6) are used, which shows ρ_{rime} as a function of liquid drop size times impact velocity $r_\ell v_o$ for several temperatures between −5° and −30°C. A value of $r_\ell v_o$ is averaged

[1] See Harrington et al. [2013a, their Eq. (16)].

over the riming rate and used to calculated $\overline{\rho}_{\text{rime}}$, which is interpolated to the ambient temperature.

For computational efficiency, values needed to calculate bulk riming rates, rime density, and liquid tendencies are computed offline and stored in a lookup table. The tables span a realistic range of liquid mixing ratios (either q_C or q_R) and the characteristic size r_n, δ_*, and ρ_I, all of which are log spaced except δ_*, which spans a range from 0.55 to 1.4 and is linearly spaced. Bulk riming rates and the average $r_\ell v_o$ needed to calculate $\overline{\rho}_{\text{rime}}$ are tabulated in this way for cloud and rain. Since rain number concentration is also prognosed, rain number tendencies due to riming are also tabulated.

To model shape evolution during riming, δ_{rime} must be estimated, and observations are used. As a result of ice particle orientation during sedimentation, only one axis is generally observed to collect rime, provided the particle has sufficient eccentricity to maintain its fall orientation (Heymsfield 1982). Using these observations, we assume that for oblate (prolate) ice $\delta_{\text{rime}} \to \infty$ ($\delta_{\text{rime}} \to 0$). In other words, riming extends only the minor axis until the axis ratio reaches a limiting value. Aspect ratios of fully developed graupel are almost never unity, and observations show they are actually closer to 0.8 (Heymsfield 1977). Therefore, in ISHMAEL oblate ice evolves towards a limiting $\phi_I = 0.8$ and prolate ice towards the inverse of this value (1.25) during riming.

When wet growth conditions occur [Lamb and Verlinde (2011), p. 474, their Eq. (12.13)] riming is assumed to increase the density of ice through water soaking into ice as opposed to freezing and extending an axis length (Mansell et al. 2010; Morrison and Milbrandt 2015). Therefore, ρ_I increases during wet growth by increasing q_I at constant V_I. If ρ_I reaches the density of bulk ice $\rho_b \approx 920\,\text{kg}\,\text{m}^{-3}$, the axis lengths grow, as no more soaking can occur.

3) MELTING

The rate of melting for a single ice particle comes from Lamb and Verlinde [2011, p. 374, their Eq. (8.85)], with the addition of the sensible heating term from collected cloud droplets and rain (Wisner et al. 1972; Milbrandt and Yau 2005b). The bulk integration of the melting rate equation is done analytically following Kong and Yau [1997, their Eq. (42)], and is integrated over the size distribution. The melt density is assumed to be that of liquid water $\rho_{\text{melt}} = \rho_w = 1000\,\text{kg}\,\text{m}^{-3}$. This method provides a simplified way to account for liquid fraction on ice without adding another prognostic variable. Number loss during melting is assumed to be proportional to w_{melt} like sublimation [Eq. (23)].

Ice shape evolution for single particles during melting has been observed (Knight 1979; Fujiyoshi 1986; Mitra et al. 1990) and modeled (Kintea et al. 2015), but no theory exists to evolve shape in a bulk model. Our parameterization is therefore based on the general changes that occur to ice as it melts based on observations. As an ice particle melts, water pools towards the center, which makes the particle more isometric, increases the density, and increases the fall speed (Lamb and Verlinde 2011, p. 369). Because melting occurs at the tips and branches of ice particles first, letting $\delta_{\text{melt}} = \delta_*$ is arguably a good approximation. For instance, when particles are oblate and $\delta_* < 1$, melting will occur initially along the a axis of the particle. As melting continues, ice generally becomes more isometric as the density increases, especially after the ice structure begins to collapse and water pools to the center. The transition to isometric ice tends to occur rapidly, though no general observations of this shape transition exist as a useful guide for an analytical model. To mimic, to first approximation, the rapid transition to isometric meltwater, the following procedure is employed: Once the density reaches $700\,\text{kg}\,\text{m}^{-3}$, the melt along the major axis is assumed to pool along and extend the minor axis. The amount the minor axis is extended is linearly weighted as a function of ρ_I from 700 to $920\,\text{kg}\,\text{m}^{-3}$, where, as ρ_I increases, there is less empty space for meltwater to occupy, and therefore the minor axis is extended more. Tests (section 4) indicate that this produces a densification, an isometrification, an increase in fall speed, and appropriate changes in mass-weighted diameter.

4) NUCLEATION

Heterogeneous ice nucleation (deposition nucleation, contact freezing, and immersion freezing of cloud droplets) is parameterized using the method of DeMott et al. (2010), where the nucleation rate is proportional to T and the number of sufficiently large aerosol particles. The number of large aerosols as a function of height comes from Chagnon and Junge (1961). For simplicity, cloud- and raindrops are homogeneously frozen at temperatures below −35°C. Immersion freezing of raindrops comes from Bigg (1953). The rime splintering rate comes from Hallett and Mossop (1974). Mass and number mixing ratio tendencies for these processes are computed as bulk quantities. When raindrops collide with ice, if the binned-rain fall speed is faster than the binned-ice fall speed, the collision process is assumed to freeze raindrops when $T < 273.15\,\text{K}$. Mass and number mixing ratio tendencies from this process are calculated and stored in a lookup table. The nucleation density for all processes is ρ_b.

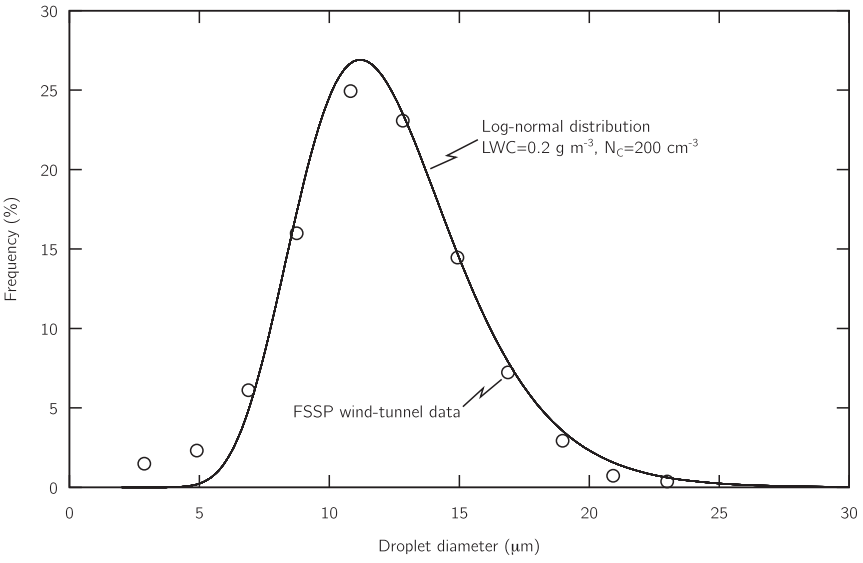

FIG. 2. Frequency of cloud droplets of various diameters as measured in a wind tunnel by an FSSP (open circles) and a lognormal fit to the data. Wind tunnel data are from Takahashi and Fukuta (1988).

5) AGGREGATION

Bulk aggregation mass and number mixing ratio tendencies are calculated for all cross- and self-collection following Walko et al. (1995) and Meyers et al. (1997) for number and mass, but with modifications for density and aspect ratio to prevent hail-like ice from producing aggregates. For a collection event involving q_α and q_β, where α and β can be 1, 2, or 3, self-collection occurs when $\alpha = \beta$, and cross-collection occurs when $\alpha \neq \beta$. The temperature-dependent collection efficiency E_{II} is multiplied by two factors f_ρ and f_ϕ, which both vary between 0 and 1. These factors reduce the value of E_{II} as ice becomes denser and more spherical, ensuring that graupel-like and hail-like ice do not produce abundant aggregates. Limits on the density and the particle shape ($\varepsilon = \phi_I$ for oblate and $\varepsilon = \phi_I^{-1}$ for prolate, so that $\varepsilon \leq 1$) of $400\,\mathrm{kg\,m^{-3}}$ and 0.1, respectively, are used to define f_ρ and f_ϕ, where

$$f_\rho = \begin{cases} \dfrac{\rho_b - \max(\rho_\alpha, \rho_\beta)}{\rho_b - 400\,\mathrm{kg\,m^{-3}}}, & \text{if} \quad \max(\rho_\alpha, \rho_\beta) > 400\,\mathrm{kg\,m^{-3}} \\ 1, & \text{if} \quad \max(\rho_\alpha, \rho_\beta) \leq 400\,\mathrm{kg\,m^{-3}}, \end{cases} \tag{25}$$

and

$$f_\phi = \begin{cases} \dfrac{1 - \max(\varepsilon_\alpha, \varepsilon_\beta)}{1 - 0.1}, & \text{if} \quad \max(\varepsilon_\alpha, \varepsilon_\beta) > 0.1 \\ 1, & \text{if} \quad \max(\varepsilon_\alpha, \varepsilon_\beta) \leq 0.1, \end{cases} \tag{26}$$

The above factors, though ad hoc, ensure that if the average ice density or aspect ratio of any ice species involved in self- or cross-collection are $\rho_I > 400\,\mathrm{kg\,m^{-3}}$ or $0.1 < \phi_I < 10$, respectively, the collection efficiency will be reduced. The density at which f_ρ becomes less than unity corresponds to a typical graupel density in traditional models. Aggregation efficiencies should decrease with increasing density for unrimed ice as well because higher-density unrimed ice particles have fewer branches to interlock. The aspect ratio at which f_ϕ becomes less than unity is an order of magnitude on either side of spherical to reduce the collection efficiencies for thick planar ice, thick columns, and rimed ice.

f. *Ice fall speeds*

Mass- (v_{t_I}) and number-weighted ice fall speeds are calculated following the method of Harrington et al. (2013a); a number-weighted Best number is used to determine the Best number–Reynolds number fit from Mitchell and Heymsfield (2005). The fall speed is then determined from the Reynolds number, and this fall speed formulation is integrated over the size distribution appropriately mass or number weighted. The volume variables are assumed to fall at the same speed as the mass: the mass-weighted fall speed is used to calculate the sedimentation of ϑ_I and ψ_I.

4. Bulk riming and melting parameterization tests

The parameterization described above is unique in that the mass, average aspect ratio, average density, and

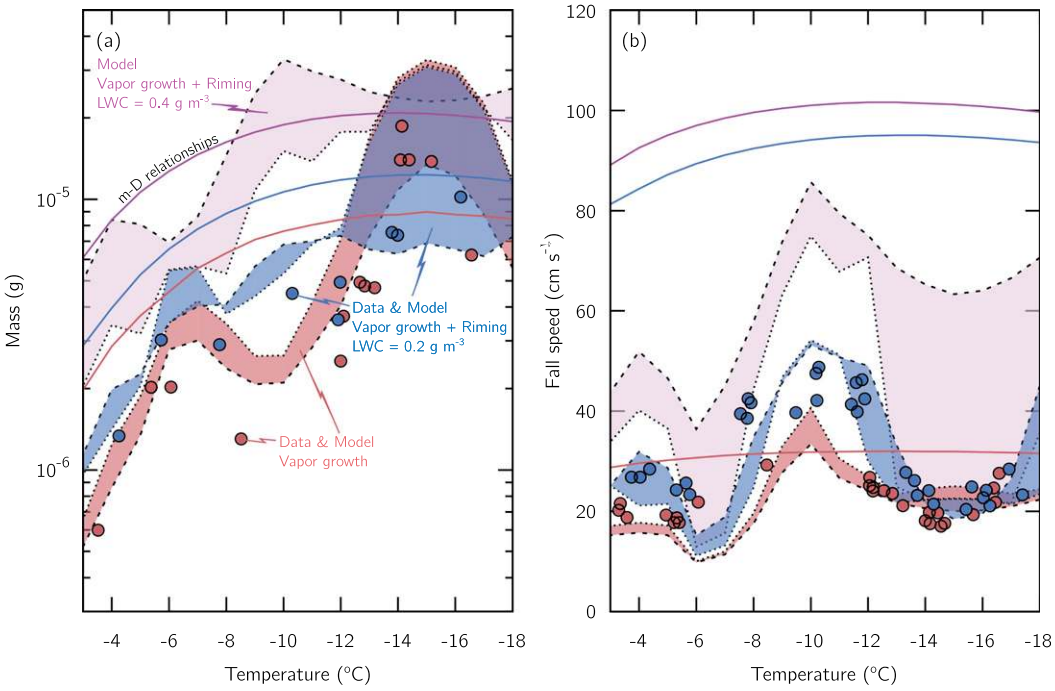

FIG. 3. (a) Mass versus temperature at 15 min of growth by vapor deposition (red shaded region), vapor deposition and riming with LWC = $0.2\,\mathrm{g\,m^{-3}}$ (blue shaded region), and vapor deposition and riming with LWC = $0.4\,\mathrm{g\,m^{-3}}$ (mauve shaded region). The shaded regions represent the spread in solution from $\nu = 4$ (dashed lines) to 12 (dotted lines). Wind tunnel data at 15 min for vapor growth are filled red circles (Takahashi et al. 1991) and for vapor growth and riming are filled blue circles (Takahashi and Fukuta 1988). Also plotted are model results using *m–D* relationships for vapor growth (red solid line), vapor growth and riming with LWC = $0.2\,\mathrm{g\,m^{-3}}$ (blue solid line), and vapor growth and riming with LWC = $0.4\,\mathrm{g\,m^{-3}}$ (mauve solid line). (b) As in (a), but for fall speed versus temperature. Coefficients used for *m–D* and v_t–*D* relationships are discussed in the appendix.

average maximum dimension of ice particles evolve during vapor growth, sublimation, riming, and melting. The parameterization for vapor growth and sublimation was tested against binned microphysical model simulations and wind tunnel data in a prior paper (Harrington et al. 2013b). Similar tests are conducted here of the bulk riming parameterization in comparison to wind tunnel data from Takahashi and Fukuta (1988) and Takahashi et al. (1991). Laboratory-based tests of the melting parameterization are not possible since, to our knowledge, no laboratory data sufficient for model testing exist for the melting of nonspherical ice. To indicate the method's numerical accuracy, it is tested against a binned melting calculation in parcel simulations.

a. Bulk riming parameterization comparison with wind tunnel data

To best compare the bulk riming parameterization with wind tunnel data, the modeled droplet distribution properties must match the measured wind tunnel distribution properties. The cloud-droplet distributions measured in the wind tunnel by a forward scattering spectrometer probe (FSSP) were relatively narrow, with most diameters being less than 20 μm (Takahashi and Fukuta 1988). If we are to assume a constant number concentration in the model, using a liquid water content (LWC) of $0.2\,\mathrm{g\,m^{-3}}$ produces a cloud-droplet distribution that matches the wind tunnel data (Fig. 2). Comparison with wind tunnel data is performed at 15 min of growth using LWCs of 0.2 and $0.4\,\mathrm{g\,m^{-3}}$. Several simulations are performed, using a box model (Sulia and Harrington 2011) with one ice species, across a range of temperatures with no vertical motion, no sedimentation, constant pressure (860 hPa), and liquid saturation. Ice number concentration is set to $1\,\mathrm{L^{-1}}$, simulations are run with values of ν from 4 to 12, and the initial number-weighted mean ice radius is set to 10 μm. When the modeled LWC is $0.2\,\mathrm{g\,m^{-3}}$ the bulk simulation captures the general habit-dependent riming observed in the wind tunnel measurements across a range of distribution shape parameters. The general feature of habit-dependent riming (Jensen and Harrington 2015) seen in both the model output and wind tunnel data is that ice grown isometrically by vapor deposition (near −3° and −10°C) rimes by a fractionally larger amount than eccentric ice (e.g., dendrites at −15°C): note the distinct upward shift

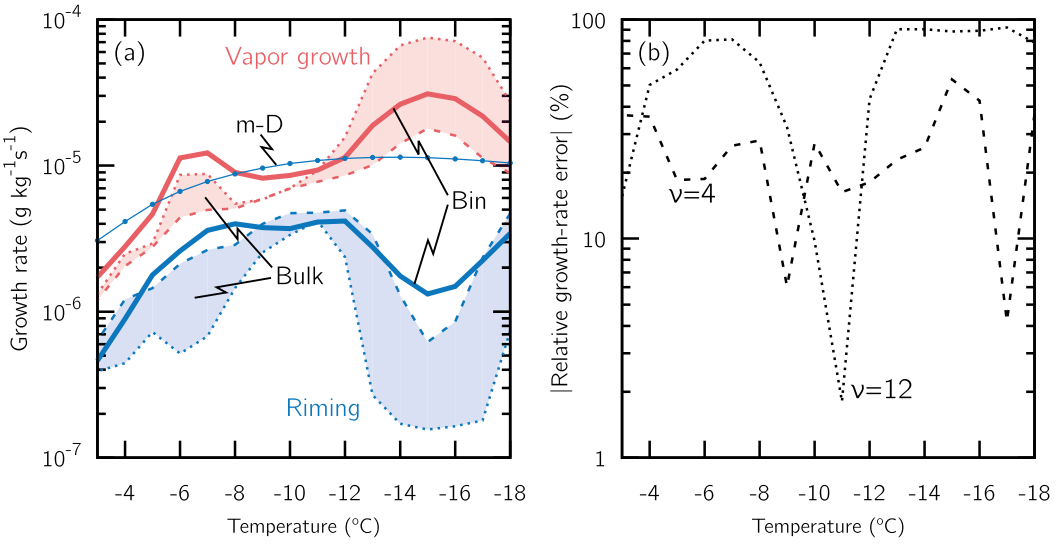

FIG. 4. (a) Vapor-depositional growth (red) and riming (blue) rates versus temperature at 15 min from the bulk model (shaded regions), the bin model (thick solid lines), and the *m–D* model (thin solid line with circles; only riming rates are shown). The shaded regions represent the parameter space from $\nu = 4$ (dashed lines) to 12 (dotted lines). (b) The absolute value of the relative errors for total bulk growth rates compared to bin-model growth rates. The dashed line is for $\nu = 4$, and the dotted line is for $\nu = 12$.

in mass near −3° and −10°C (Fig. 3a, blue vs red shaded regions). For comparison, simulations are also shown with a traditional bulk approach by using an *m–D* and v_t–*D* relationship for dendritic snow (Mitchell 1996). Using a traditional method, riming occurs at all temperatures because only one ice habit type is represented (Fig. 3a, red vs blue lines). When riming is weak, traditional models that convert snow to graupel will overpredict ice mass. As expected, the *m–D* model compares best to the wind tunnel data near where branched planar crystals grow (near −15°C). This result indicates that parameterizing habit-dependent riming with traditional approaches may be possible, but at the expense of requiring a large number of categories.

At a higher LWC, the mass predicted by ISHMAEL and the traditional model are closer, which is expected because of the faster graupel production (Fig. 3a, mauve shaded region vs mauve solid line). Consequently, traditional bulk schemes and models that predict particle properties should produce relatively similar results when riming rates are large.

The variation of fall speed with temperature (habit) is reproduced by ISHMAEL, including the fall speed increase due to riming (Fig. 3b). At moderate LWCs, dendrites rime weakly, and hence their fall speed is not increased. However, isometric ice (near −10°C) rimes rapidly, so the fall speed increases commensurately. In contrast, graupel forms instantaneously in many traditional models, and this drastically increases fall speed over that of snow, amplifying the riming rate. This feedback between fall speed increase and riming rate can lead to an overprediction of mass and fall speed in a traditional model.

Bulk models often fix the distribution shape, and this has important consequences for the simulated microphysical processes. Isometric ice (−10°C) rimes faster for smaller values of ν, because of the more prominent distribution tail (Fig. 3a, blue region; dashed vs dotted lines). Dendrites, on the other hand, are just beginning to rime at an LWC of 0.4 g m^{-3}, and therefore decreasing ν will increase the tail of the ice distribution leading to the relatively large change in fall speed near −15°C (Fig. 3b, mauve shaded region).

b. *Bulk riming parameterization comparison with a bin model*

The value of ν used in ISHMAEL demonstrably alters the process rates; the choice of ν is facilitated by comparing the bulk model with the adaptive-habit Lagrangian bin model of Sulia and Harrington (2011) employing 200 bins. These simulations use the same setup as section 4a (15 min of growth with an LWC of 0.2 g m^{-3}). The clear temperature dependence of mass shown in Fig. 3a is also apparent in the vapor growth and riming rates for a range of ν (Fig. 4a). Employing $\nu = 4$ produces the lowest total (vapor growth plus riming) growth rate error with respect to the bin model (Fig. 4b), similar to what was found by Milbrandt and Yau (2005a). As expected, over-riming occurs at all temperatures when

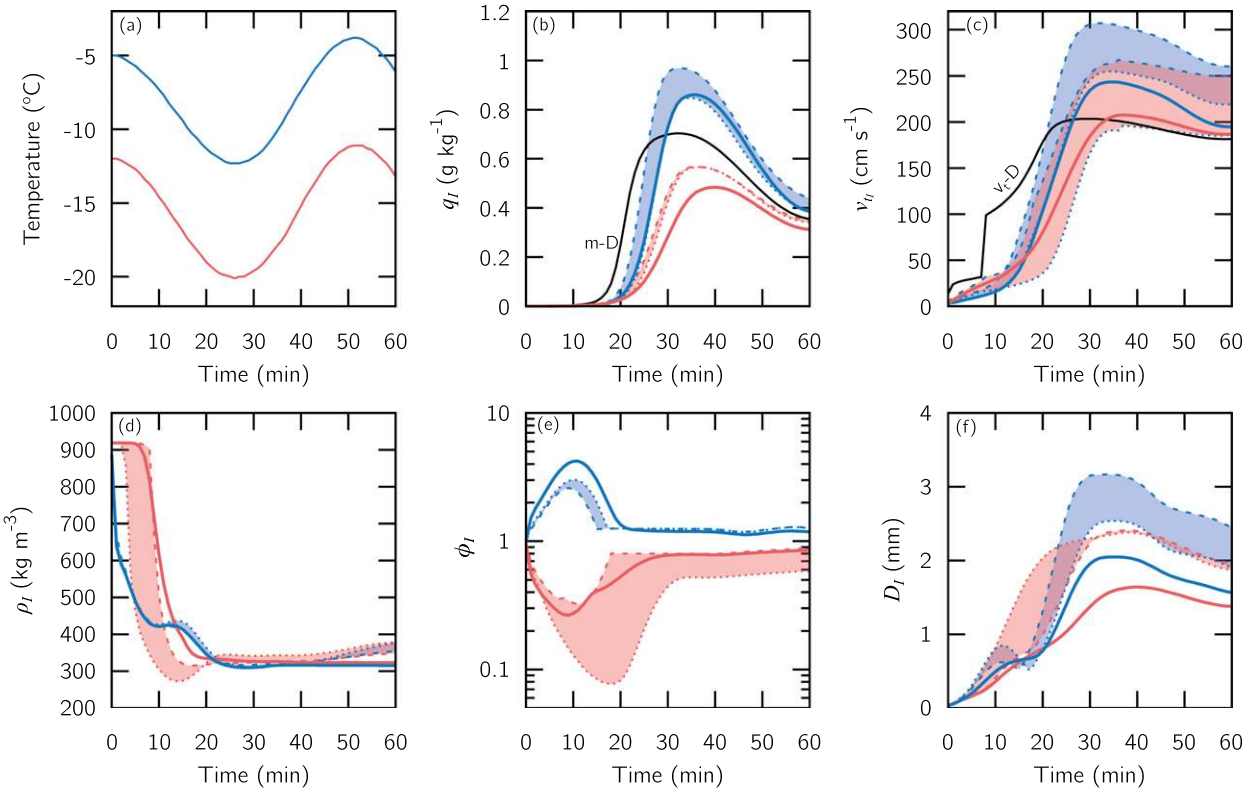

FIG. 5. (a) Temperature, (b) ice mass mixing ratio, (c) mass-weighted fall speed, (d) volume-weighted density, (e) number-weighted aspect ratio, and (f) mass-weighted maximum diameter from the bin model (solid colored lines), the bulk model (shaded colored regions), and the *m–D* model (black lines; only ice mass and fall speed are shown). See Fig. 3 for an explanation of the shaded regions.

using an *m–D* relationship to characterize ice (Fig. 4a, thin blue line with dots).

c. *Bulk ice property evolution during vapor growth and riming*

The comparisons above are for a range of simulations using a fixed temperature and thus a fixed value of δ_{dep}; it is therefore natural to ask how well the bulk model performs, compared with the bin model, when temperature changes. To assess this, sinusoidally varying vertical motion with an amplitude of 1 m s^{-1} is included in the parcel model, with a model depth of 1 km. Relative humidity and pressure are initialized at 98% and 900 hPa, respectively. Two different temperature regimes are used: one supporting planar ice growth and one supporting columnar ice growth.

Compared with the bin model, ISHMAEL captures the evolution of ice mass mixing ratio, mass-weighted fall speed, volume-weighted density, number-weighted aspect ratio, and mass-weighted maximum diameter $D_I = 2\max(a_I, c_I)$ [Eq. (20)] over an up- and downdraft cycle (Fig. 5). The greatest discrepancy between the bulk and bin models is in the mass-weighted maximum dimension and is a result of fixing the bulk distribution shape. Importantly, the bulk model evolves average aspect ratio for both oblate and prolate ice by both vapor deposition and riming, capturing the transition to isometric ice (Fig. 5e, blue and red shaded regions). As ice rimes and becomes isometric, the fall speed rapidly increases over approximately 10 min for both habits (Fig. 5c). Employing a traditional v_t–*D* relationship does not allow a natural fall speed transition from snow to graupel; instead, the fall speed instantaneously becomes graupel-like (Fig. 5c, solid black line). A delay in the conversion from snow to graupel *m–D* and v_t–*D* relationships could be used to better match the ISHMAEL model (Fig. 5b; cf. solid black and solid red lines), but doing so would involve tuning the model threshold for the conversion.

d. *Bulk melting parameterization comparison with a bin model*

The accuracy of the bulk melting parameterization is tested against a bin model. In these simulations, planar ice, columnar ice, and graupel-like ice with different initial number concentrations melt at 0.5°C. For all simulations, the bulk ice mass (Fig. 6a) and number (Fig. 6b) mixing ratios remain larger than the bin values. Density increases as melting progresses

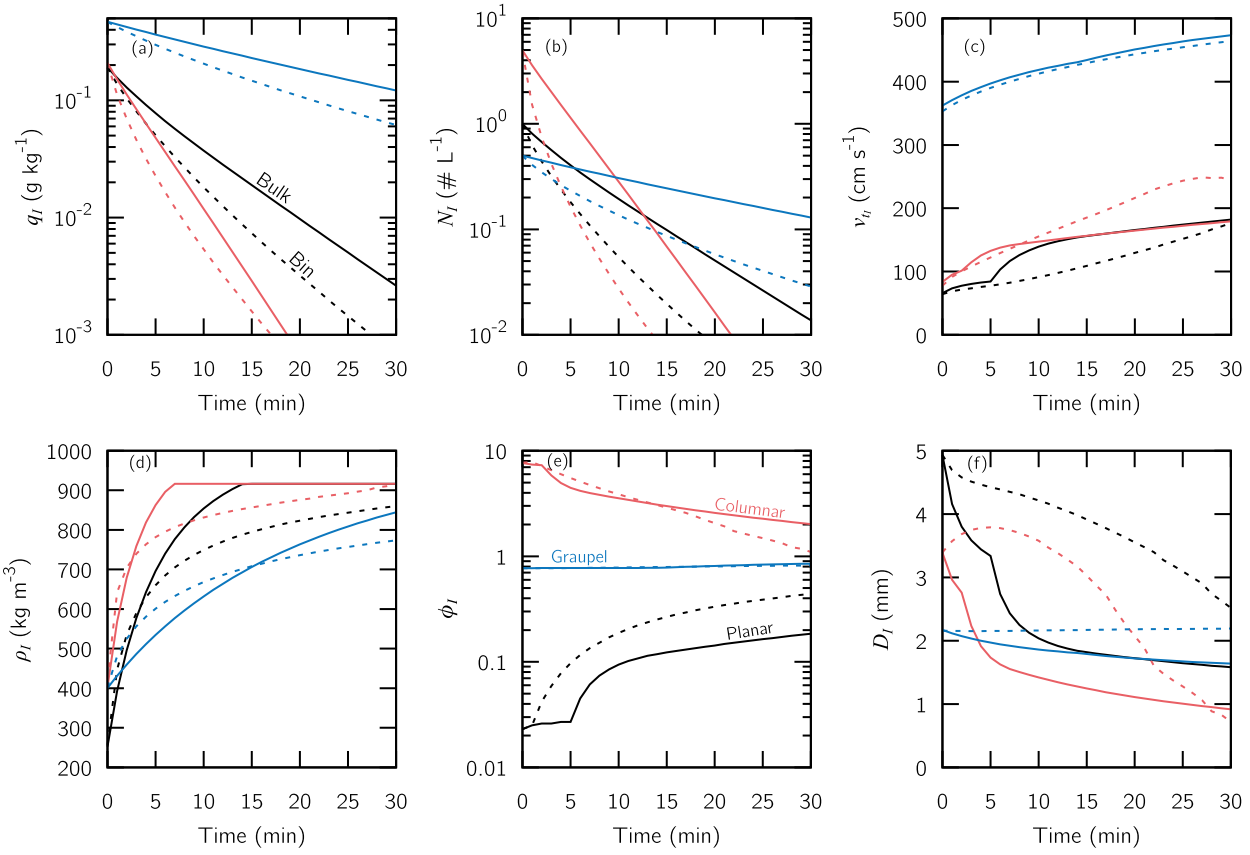

FIG. 6. (a) Ice mass mixing ratio, (b) ice number concentration, (c) mass-weighted fall speed, (d) volume-weighted density, (e) number-weighted aspect ratio, and (f) mass-weighted maximum diameter from the bin model (dashed lines) and the bulk model (solid lines) during melting of planar ice (black), columnar ice (red), and graupel (blue).

(Fig. 6d), and the number-weighted aspect ratio becomes more isometric (Fig. 6e). These changes in ice properties lead to an increase in fall speed (Fig. 6c). The mass-weighted maximum diameter decreases more rapidly in the bulk model compared with the bin model for each simulation (Fig. 6f). This underprediction in maximum dimension is due to the relatively large overprediction in number concentration (mass, number, density, and axis length are consistently related). All bulk variables have the correct trend compared with the bin calculations except the maximum dimension: because the bulk distribution shape is fixed, the bulk maximum dimension monotonically decreases, while it can increase in the bin simulations. For example, in the bin model, when graupel melts, the maximum diameter remains approximately constant (Fig. 6f, dashed blue line). This is because the complete melting of small graupel, which leads to a larger average size, is balanced by the decrease in the size of ice that partially melts. While more work is needed to better parameterize ice property evolution during melting, the current approach provides an approximate method that captures the general features of habit-dependent melting.

5. Kinematic modeling demonstrations with ISHMAEL

ISHMAEL is compared to a traditional model, the Milbrandt and Yau two-moment microphysics (MY2; Milbrandt and Yau 2005a,b), to indicate whether it is reasonably handling the overall evolution of condensate mass and number and to indicate where we may expect to find the largest impacts of evolving particle shapes as compared to traditional schemes.

a. The kinematic model setup

A 2D kinematic framework (Szumowski et al. 1998) is used to demonstrate the capabilities of ISHMAEL. Kinematic models have prescribed flow fields and do not include feedbacks between the microphysics and dynamics so that the effects of microphysical processes can be isolated. The thermodynamic structure (Fig. 7a) used to initialize the model is based on soundings taken

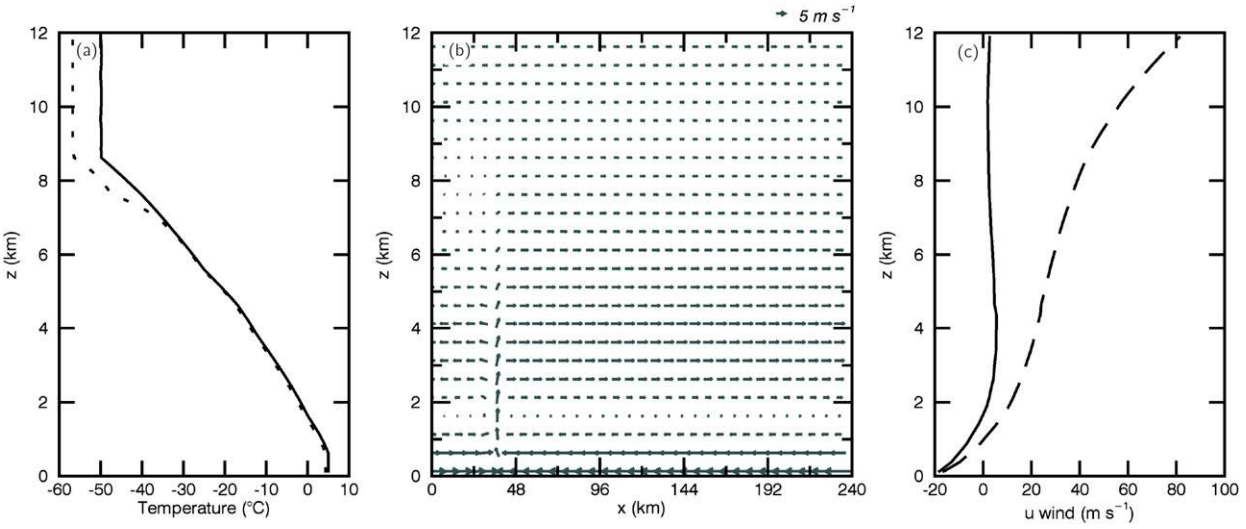

FIG. 7. Vertical profiles of (a) temperature (solid) and dewpoint (dashed) used in the kinematic simulations. (b) Wind vectors plotted for the LS case with $w_{max} = 5\,m\,s^{-1}$. The w component of the vectors is doubled to highlight the location of the updraft. (c) The LS (solid) and HS (dashed) u-wind vertical profiles (plotted at $x = 150$ km) used in the kinematic model.

during the second Improvement of Microphysical Parameterization through Observational Verification Experiment (IMPROVE-2) campaign (see Garvert et al. 2005). The wind field consists of an updraft that is approximately 10 km wide with a maximum value w_{max} embedded in a horizontal flow (Fig. 7b). Simulations are run for 6 h, and for the first 15 min the updraft is sinusoidally increased from $0\,m\,s^{-1}$ to w_{max} and held constant at w_{max} until 4 h, and then from 4 to 4.5 h the updraft is sinusoidally spun down to naught. The horizontal grid spacing is 750 m, the vertical grid spacing is 250 m, and the domain is 12 km high by 240 km wide. Advection is calculated using the multidimensional positive definite advection transport algorithm (MPDATA; Smolarkiewicz 1984; Smolarkiewicz and Margolin 1998).

Simulations are run using two different u-wind profiles (Fig. 7c): one with low vertical wind shear (LS) and one with high vertical wind shear (HS). The HS case represents an idealized orographic event: strong rising motion over a barrier lofts hydrometeors into a horizontal flow that carries them downwind. The LS case represents a towering cumulus, and is used to study the vertical distribution of hydrometeors when horizontal advection of hydrometeors is weak. Two different updraft intensities, $w_{max} = 1\,m\,s^{-1}$ and $w_{max} = 5\,m\,s^{-1}$, are employed in the LS and HS environments to study how changing the dynamical forcing influences hydrometeor distributions. The four model setups used are therefore LS1, HS1, LS5, and HS5, where the number corresponds to the value of w_{max}.

Comparison to MY2 uses their cloud ice, snow, and graupel categories; the mass mixing ratios of these categories are q_i, q_s, and q_g, respectively. In the version of MY2 used, if the amount of rime $\Delta q_{s,rime}$ for snow is greater than the vapor-depositional growth, then the amount of conversion from snow to graupel is $\Delta q_{s,rime}[(100\Delta q_{s,rime})/q_s]$. Note that if $\Delta q_{s,rime}$ is greater than 1% of q_s, some snow mass along with all of the rime mass is converted to graupel. Sensitivity studies (not shown) using another method of conversion where the amount of mass converted from snow to graupel is based on the density difference between the snow and graupel categories (Murakami 1990; Milbrandt and Yau 2005b) do not change the results below.

b. *Ice species property evolution in the kinematic model*

The different ice species used in ISHMAEL complicate how ice will be sorted vertically and horizontally in a cloud system because the fall speed of each ice species depends on how ice properties of that species evolve. The lack of predefined snow and graupel categories in ISHMAEL requires analysis of ice properties for direct comparison to

TABLE 2. General ice properties used to diagnose ice type.

Ice type	ϕ_I	ρ_I (kg m^{-3})	v_{t_I} (m s^{-1})
Oblate (planar)	<1		
Prolate (columnar)	>1		
Graupel	$0.8 < \phi_I < 1.25$	<600	>1
Densely rimed (planar) ice	$0.5 < \phi_I < 0.8$	<600	
Unrimed, branched ice	<0.1	<700	<1
Cloud ice		>700	<0.5

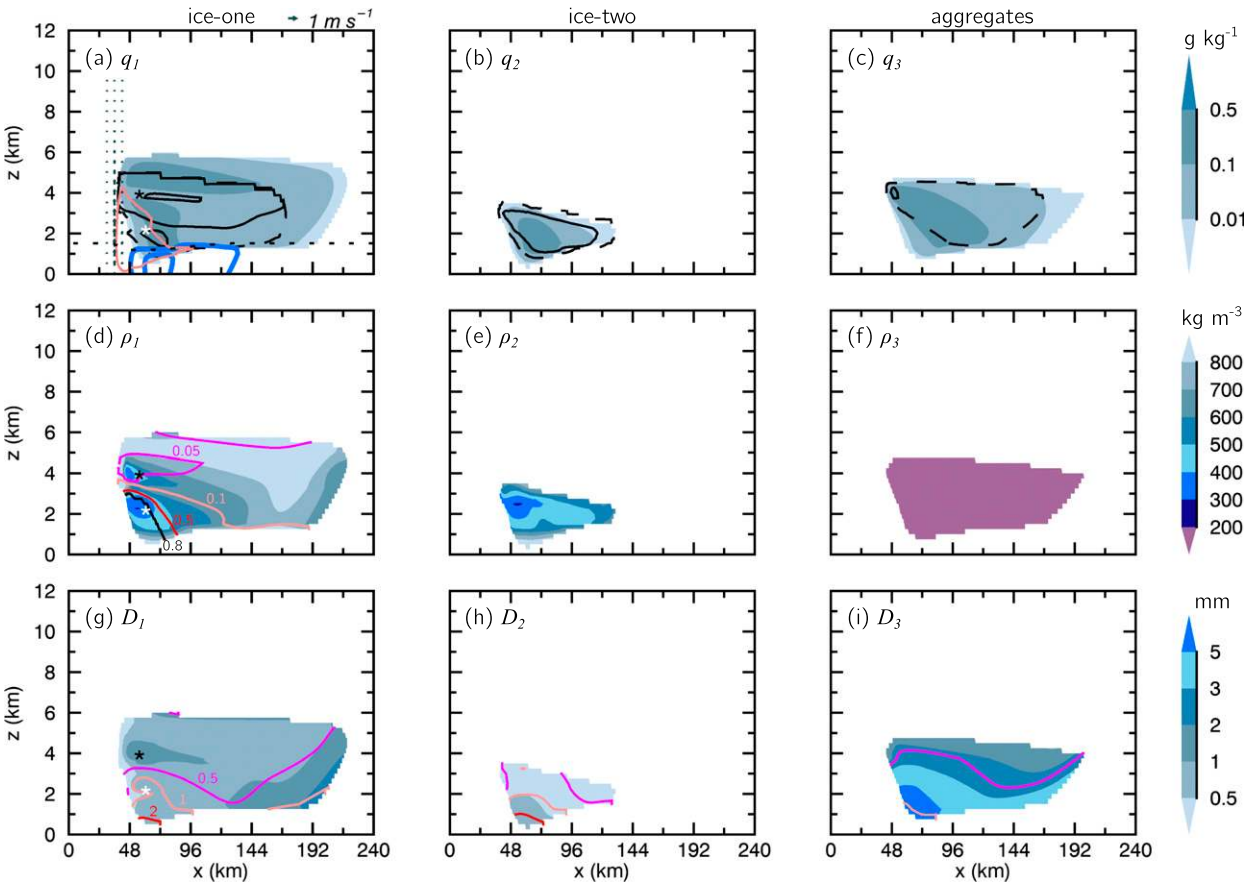

FIG. 8. Ice properties (plotted where $q_I > 0.001\,\mathrm{g\,kg^{-1}}$) for each species at 2 h from the HS1 simulation. (a)–(c) Mass mixing ratio (shaded) and number concentration [black contours; intervals are 1 (dashed line) and $10\,\mathrm{L^{-1}}$ (solid line)]. Also shown in (a) is the updraft (gray arrows), cloud water (salmon contour; interval is $0.1\,\mathrm{g\,kg^{-1}}$), and rainwater (blue contours; intervals are 0.01 and $0.1\,\mathrm{g\,kg^{-1}}$). (d)–(f) Volume-weighted density (shaded) and number-weighted aspect ratio [solid contours; intervals are 0.05 (magenta), 0.1 (salmon), 0.5 (red), and 0.8 (black)]. The range in number-weighted aspect ratio in (e) is $0.8 < \phi_2 < 1.25$ and $\phi_3 = 0.2$. (g)–(i) Mass-weighted maximum diameter (shaded) and mass-weighted fall speed [solid contours; intervals are 0.5 (magenta), 1 (salmon), and $2\,\mathrm{m\,s^{-1}}$ (red)]. The ice properties located at the asterisks are discussed in the text.

other models. Snowlike and graupel-like ice is produced by the model, but those ice categories do not explicitly exist. Therefore, when we speak of snow or graupel, we are only diagnosing these ice types based on the predicted ice properties. Some general guidelines for the properties of ice used to determine ice type are listed in Table 2.

1) THE HS1 CASE

Examining ice properties from the HS1 case at 2 h, ice habits sort based on temperature-dependent nucleation as well as the dominate growth processes. The maximum in q_1 (Fig. 8a, shaded contours) extends in two directions. Ice nucleated as ice one above 4 km (−15°C) gets advected laterally from the updraft, while ice one below 4 km extends vertically toward the surface. The dominant growth process causes this vertical distribution of ice one. For example, ice near the updraft (white asterisks) in Fig. 8 is nearly isometric (Fig. 8d), falling $1–2\,\mathrm{m\,s^{-1}}$ (Fig. 8g), with a maximum diameter 0.5–1 mm (Fig. 8g) and a density between 300 and $400\,\mathrm{kg\,m^{-3}}$ (Fig. 8d). This ice, coexisting with cloud water (Fig. 8a, salmon contour) has the properties of small graupel. In contrast, at $z = 4\,\mathrm{km}$ ($T \approx -15°\mathrm{C}$, black asterisks) ice one has evolved to become unrimed, branched particles with $\phi_1 < 0.05$, $v_{t_1} < 0.5\,\mathrm{m\,s^{-1}}$, $D_1 = 1 - 2\,\mathrm{mm}$, and $\rho_1 = 400 - 500\,\mathrm{kg\,m^{-3}}$. Above 5 km, small, high-density ice dominates.

Ice two is nucleated from −5° to −9°C (2.5–3.5 km), which confines its vertical extent to below 4 km. A large source for this ice is rime splinters, which leads to number concentrations generally being larger than $10\,\mathrm{L^{-1}}$ (Fig. 8b, solid black contour). Ice two coexists with significant cloud water; thus, it rimes and becomes nearly isometric with maximum diameters less than 1 mm (Fig. 8h) and densities generally less than $500\,\mathrm{kg\,m^{-3}}$ (Fig. 8e). While this graupel is small, as pointed out in

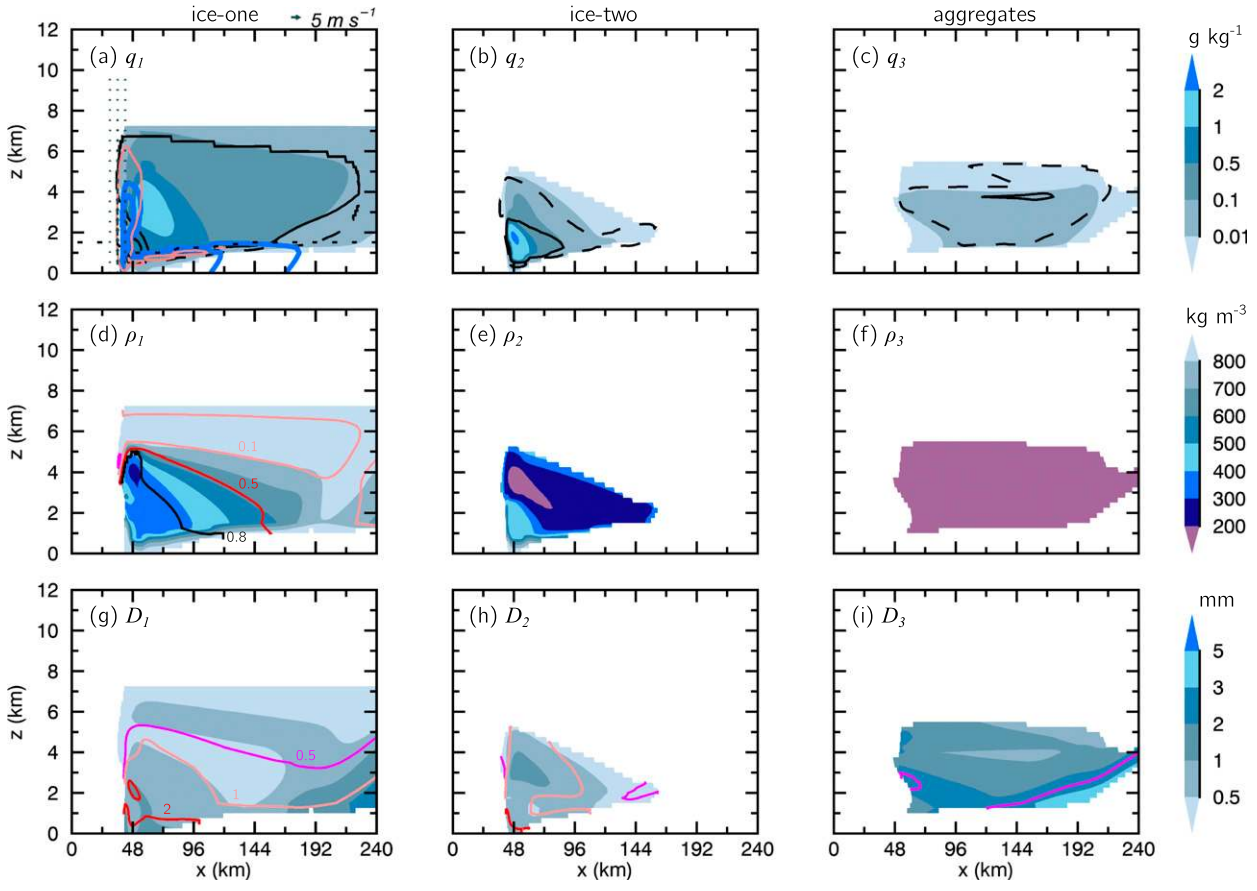

FIG. 9. As in Fig. 8, but from the HS5 simulation.

Wang and Ji (2000), columnar ice can begin riming when it reaches a maximum diameter of 70 μm.

Aggregates begin to form near the −15°C level where unrimed, branched planar ice grows. This region is conducive to aggregation, thus leading to a maximum in aggregate number concentration there of 10 L^{-1} (Fig. 8c, solid black contour). The maximum of D_3 evolves to be slightly larger than 5 mm (Fig. 8i). The fall speed of the largest aggregates just exceeds 1 m s^{-1} as some of these aggregates lightly rime.

2) THE HS5 CASE

There are a few impacts on particle properties from increasing the forcing, though in general habits sort similarly comparing HS5 (Fig. 9) with HS1. For example, the properties of ice two are similar (compare Figs. 8 and 9, column 2), though in HS5 ice two has a larger vertical extent and grows to be larger, faster falling, and with lower density than in HS1. The stronger updraft also produces rimed planar ice to a vertical extent of 5 km (Fig. 9d, where $\phi_1 \approx 1$). For both ice one and ice two, the largest rimed ice survives below the melting level, and as this ice melts the density (Figs. 9d,e) and fall speed (Fig. 9g,h) increase.

Above 5 km, aspect ratio, size, and fall speed of ice one significantly decrease, while density increases, signifying the transition to cloud ice. Notably, riming encompasses the region of dendritic growth (4 km), and, hence, formation of aggregates is suppressed as the aggregate mixing ratio remains less than 0.1 g kg^{-1}. Aggregates in HS5 are smaller and slower falling across the domain than in HS1.

c. *Spatial precipitation controls and sensitivities in ISHMAEL*

1) ASPECT RATIO SORTING

In both HS1 and HS5, ISHMAEL produces a large variation in particle properties across the domain for ice one. In the HS1 simulation, ice one alone evolves to be small, high-density "cloud ice"; unrimed, branched "snow"; and small "graupel." ISHMAEL captures various degrees of riming, as indicated by a general decrease in planar-ice aspect ratio away from

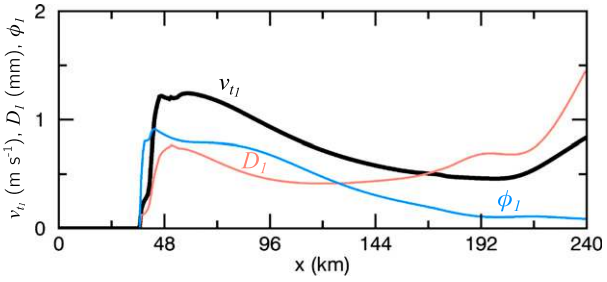

FIG. 10. Ice properties of q_1 at $z = 3.5$ km from the HS5 simulation. Plotted are mass-weighted fall speed (black), number-weighted aspect ratio (blue), and mass-weighted maximum diameter (salmon).

the main updraft (Figs. 8d, 9d). In HS5, a significant fraction of ice one exists as graupel and densely rimed ice with $0.5 < \phi_1 < 0.8$ (Fig. 9d). A consequence of representing partially rimed ice is that this ice is sorted in physical space by aspect ratio in a process similar to Chen and Lamb (1999): because the degree of riming controls ice particle thickness and density and hence fall speed, faster falling, highly rimed ice remains near the updraft, whereas more pristine ice is advected away. Indeed, in the HS5 case, ice one fall speeds decrease commensurately with aspect ratio (Fig. 10), a result supported by observations that show thicker or sectored plates have higher fall speeds than stellar or dendritic particles (Kajikawa 1972; Locatelli and Hobbs 1974). Mass and aspect ratio are tied to fall speed through gravity and drag (Böhm 1989; Mitchell 1996; Mitchell and Heymsfield 2005); thickening of particles during riming increases mass without significantly increasing drag, and thus fall speed increases.

The process of aspect ratio sorting described above is different from size sorting, which results from mass and number mixing ratios falling with different sedimentation velocities. The advected quantities used to track shape evolution [Eqs. (11) and (12)] fall with a mass-weighted fall speed; therefore, aspect ratio sorting arises from diagnosing mass-weighted fall speed as a function of shape. Aspect ratio sorting is natural, as the degree of riming is controlled by the particle properties, unlike the somewhat artificial sorting produced by conversion between categories in tradition schemes. Unless aspect ratio and density evolve, fall speeds of transitional particles during riming cannot be captured. Among the ice particle properties that indubitably affect fall speed, aspect ratio and density evolution are generally missing from models. One consequence of parameterizing aspect ratio sorting is that it affects the spatial precipitation distribution as compared to a traditional modeling approach. The 6-h accumulated precipitations for both the HS1 and HS5 cases (Fig. 11a) show that MY2 consistently produces precipitation over a larger spatial range than ISHMAEL. Accumulated precipitation monotonically decreases with distance away from the updraft for ISHMAEL, while it levels off spatially in MY2.

Differences in spatial precipitation distribution between ISHMAEL and MY2 for the LS5 case (Fig. 11b, solid lines) arise because a significant portion of the updraft is rising at the same magnitude as the fall speed of small graupel (approximately 2 m s^{-1} for 2-mm-diameter graupel). The timescale to form graupel is important for the spatial precipitation distribution because faster falling graupel can fall through the center of the updraft, increasing precipitation in that location. In ISHMAEL, the transition to graupel is slow enough that a significant amount of ice advects laterally away from the updraft on both sides before it can collect enough rime to fall through the center

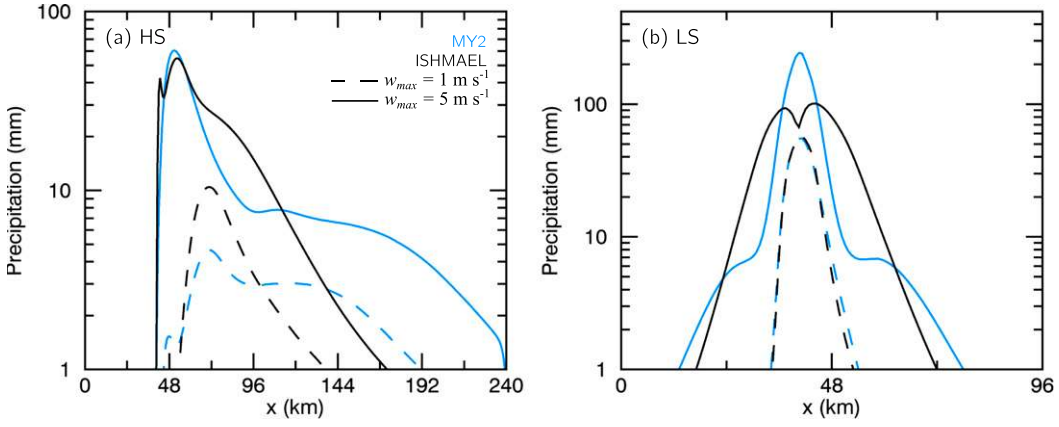

FIG. 11. (a) The 6-h accumulated precipitation from the HS1 simulation (dashed lines) and the HS5 simulation (solid lines) from ISHMAEL (black) and MY2 (blue). (b) As in (a), but from the LS1 and LS5 simulations.

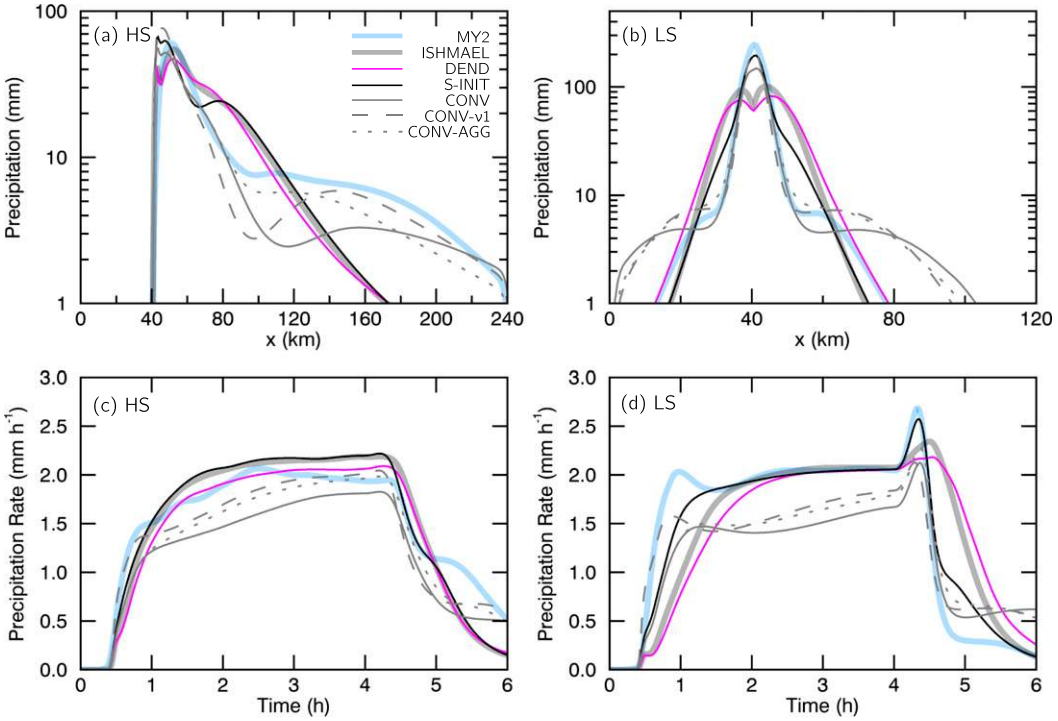

FIG. 12. (a) The 6-h accumulated precipitation from the HS5 simulation using ISHMAEL (thick solid gray) and MY2 (blue), and the 6-h accumulated precipitation from DEND (fuchsia), S-INIT (black), CONV (thin solid gray), CONV-ν1 (thin dashed gray), and CONV-AGG (dotted gray). (b) As in (a), but using the LS5 environment. (c) Domain-averaged precipitation rate for the simulations in (a). (d) Domain-averaged precipitation rate for the simulations in (b).

of the updraft, causing the bimodal spatial precipitation distribution.

2) PRECIPITATION SENSITIVITIES TO SPECIES INITIATION AND SNOW–GRAUPEL CONVERSION

Because ISHMAEL evolves particle properties in contrast to traditional schemes, we expect differences like those discussed above. However, it is not always clear as to why these differences occur. To better understand habit evolution effects on precipitation, sensitivity studies are performed using both HS5 and LS5 environments. In the first study (abbreviated S-INIT), the species initiation method in ISHMAEL is changed from being temperature dependent (oblate vs prolate) to being size dependent, where small ice (i.e., frozen cloud droplets) is nucleated to ice one, and large ice (i.e., frozen raindrops) is nucleated to ice two. The purpose of this sensitivity study is to explore the impact on precipitation of partitioning ice at nucleation based on size versus shape.

Second, in order to investigate how habit evolution affects precipitation, simulations are conducted with ice grown as dendrites (by fixing δ_{dep}). In this simulation (abbreviated DEND), all ice is nucleated to ice one, though aggregation still occurs. Finally, we attempt to mimic processes in MY2 by combining S-INIT and DEND such that small ice is nucleated to ice one and parameterized to grow as dendrites, and large ice is nucleated to ice two, but when ice one collects rime, mass and number are converted to ice two similar to MY2. In this simulation (abbreviated CONV), aggregation is off. This simulation is repeated using inverse-exponential ice distributions (CONV-ν1) and with aggregation on (CONV-AGG).

The biggest impact from the S-INIT simulations occur in the LS environment; nucleating large frozen drops in a separate category leads to faster riming and thus a monomodal spatial precipitation distribution because more ice can fall through the center of the updraft (Fig. 12b; cf. thick gray and black lines). Allowing riming to occur faster causes the precipitation rate to increase more rapidly in the early stages of the simulation (Fig. 12d, $t < 1.5$ h). The precipitation rate also increases faster and has a larger magnitude at the beginning of the updraft spindown as a result of larger water loading ($t = 4$ h). Ultimately, the larger and faster falling the graupel, the faster the response in the precipitation.

ISHMAEL and MY2 have the most similar spatial precipitation distributions when ice one is converted to ice two during riming (Figs. 12a,b; cf. thick blue to solid, dashed, and dotted gray lines). In the HS environment,

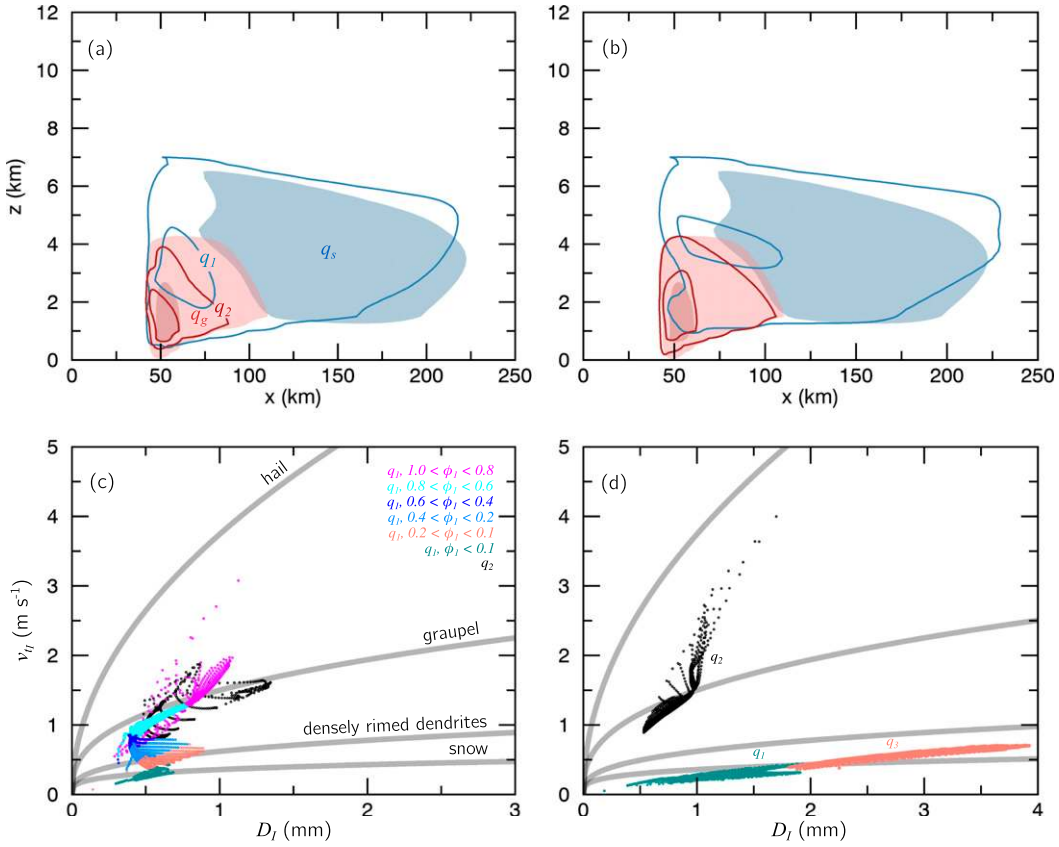

FIG. 13. Ice mass mixing ratios (contour intervals are 0.1 and 1 g kg^{-1}) from the HS5 simulation using MY2 (shaded contours; q_s is blue and q_g is red) and ISHMAEL (contour lines; q_1 is blue and q_2 is red). (b) As in (a), but instead comparing MY2 and CONV-AGG (blue contour lines are now $q_1 + q_3$). (c) Mass-weighted maximum diameter vs mass-weighted fall speed for q_1 and q_2 (from ISHMAEL) contoured in (a). Mass-weighted fall speeds for q_1 are colored by number-weighted aspect ratio. Typical v_t–D relationships are also plotted. (d) As in (c), but for q_1, q_2, and q_3 from the CONV-AGG simulation.

these simulations are the only ones that produce a tail of precipitation beyond $x = 170$ km, similar to MY2. These simulations also produce a narrow region of precipitation near the updraft that widens away from the updraft in the LS environment, again, similar to MY2. Not only does initiating conversion from snow to graupel in ISHMAEL change the spatial precipitation distribution; separating the two categories leads to a different precipitation rate evolution when the dynamics change. For example, in both the HS environment (Fig. 12c) and LS environment (Fig. 12d), after the systems spin down, the precipitation decays faster than in the other ISHMAEL sensitivity studies and then remains constant. This is caused by graupel precipitating out of the domain first, while snow precipitates out slowly from the domain.

d. *Differences between ISHMAEL and the traditional approach*

Being able to replicate the main features of spatial precipitation distribution produced by MY2 indicates that CONV, CONV-ν1, and CONV-AGG behave similarly to a traditional model. CONV-AGG produces a similar spatial precipitation distribution compared with MY2 as well as increased precipitation accumulation from $90 < x < 180$ km compared with CONV. Aggregation, which increases the size and slightly increases the fall speed of ice, occurs in MY2. It is therefore not surprising that precipitation accumulation from CONV-AGG compares well to MY2. Comparing the ice properties from both CONV-AGG and the original HS5 simulation using ISHMAEL (referred to as HS5-CTRL), the main differences between ISHMAEL and our imitation traditional model simulations are the location and properties of ice one. In HS5-CTRL, ice one evolves such that a continuum of ice types is produced. The fall speeds of this ice span a range from partially rimed ice to graupel and are sorted in physical space based on aspect ratio (Fig. 13c). In CONV-AGG, the loss of the continuum of ice types leads to some ice one becoming graupel while some remains as snow (and aggregates). Partitioning ice in

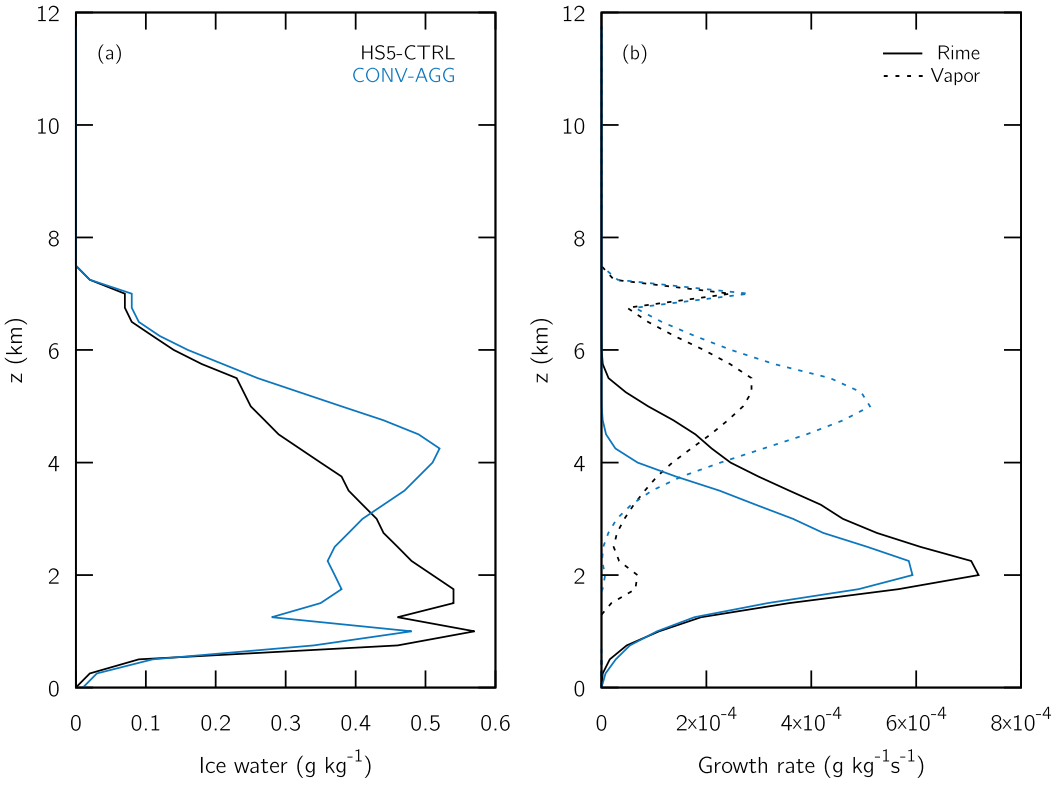

FIG. 14. (a) Total ice mass mixing ratio ($q_1 + q_2 + q_3$) averaged vertically from 2 to 3 h for grid boxes with at least 0.001 g kg^{-1} of total ice from the HS5-CTRL simulation (black) and CONV-AGG (blue). (b) Vertically averaged vapor growth (dashed) and riming (solid) rates in the updraft ($w > 0$) for HS5-CTRL (black) and CONV-AGG (blue).

this way leads to a spatial distribution of snow and graupel mixing ratio similar to MY2 (Fig. 13b). The CONV-AGG simulation also more closely matches traditional v_t–D fall speeds (Fig. 13d), even though fall speed is still diagnosed based on ice properties.

Vertically averaging ice mixing ratios from 2 to 3 h, HS5-CTRL has less total ice mass above 3 km (Fig. 14a, black line). Average riming rates in the updraft in HS5-CTRL are larger than in CONV-AGG and extend to a higher vertical level (Fig. 14b, solid lines). The local maximum in vapor growth at $z = 5$ km in HS5-CTRL is about half of the value in CONV-AGG (Fig. 14b, dashed lines). Predicting partially rimed ice ultimately leads to a reduction in vapor growth rates and an increase in riming rates near $z = 5$ km in the updraft as a result of the dependence of both growth rates on shape.

6. Discussion and conclusions

The goal of a microphysics parameterization is to capture the pertinent process rates affecting cloud systems as well as the most important ice and liquid properties. Currently, traditional approaches represent several predefined ice categories but are limited by having to choose a priori what categories to employ and by the need to convert between categories. Conversion thresholds can lead to artificial sensitivities. The advantages of predicting ice properties instead of prescribing them by employing fixed categories are that models no longer need ad hoc conversion parameterizations between categories. Instead, modeled particles retain information about prior growth conditions and therefore become dependent on and sensitive to environmental conditions and process rates, which can be constrained by theory and observation. By predicting ice properties, habit-dependent vapor growth and riming can be included in models, allowing for transitional growth states of ice. This transitional ice can have a broad range of fall speeds that impact precipitation, cloud phase partitioning, spatial location of vapor growth versus riming, and cloud system dynamics. Modeling ice transitions from vapor grown to lightly rimed and finally to densely rimed ice produces a more natural precipitation rate transition away from the convective updraft in our simulations. It also leads to a more natural system evolution when system dynamics change in time.

Shape evolution in ISHMAEL results in aspect ratio sorting, which is a process that should occur in nature but is only possible when aspect ratios evolve as a result of microphysical processes. Aspect ratio sorting leads to a different spatial precipitation distribution compared with a traditional model and will be useful to study the impacts of parameterizing ice shape evolution on mountain meteorology forecasts, including orographic precipitation events and snow–rain transition elevation, and forecasts that determine avalanche and flooding danger. These precipitation forecasts depend on the properties and process-rate parameterizations of precipitating ice (Woods et al. 2007; Minder and Kingsmill 2013). In ISHMAEL, both vapor growth and riming depend on habit. If moderate riming dominates in a region, that riming growth can suppress vapor growth (Jensen and Harrington 2015), a process that cannot be examined with traditional models. Collection efficiencies vary for different habits, and in certain environmental conditions columns and isometric habits rime while dendrites do not. We expect natural environments exist where dendrites grow by vapor growth while graupel grows through collection in the same cloud volume. Laboratory measurements show that this can happen when liquid water contents are low and liquid drop sizes are small (Takahashi and Fukuta 1988; Fukuta and Takahashi 1999). The dependence of this habit-dependent riming effect on cloud drop concentration indicates a potential impact of riming in deeper convective clouds. Particle property methods represent an advancement over traditional schemes in their ability to parameterize cloud microphysics processes and can provide insights into the impacts of microphysics on cloud systems.

Acknowledgments. The authors are grateful for the comments provided by three anonymous reviewers. The authors thank W. Grabowski for providing the original kinematic code. This research was supported by the U.S. Department of Energy's Atmospheric Science Program Atmospheric System Research, an Office of Science, Office of Biological and Environmental Research program, under Grants DE-FG02-05ER64058 and DE-SC0012827 as well as an NSF-AGS Postdoctoral Research Fellowship (AGS-1524267). The NCAR ASP visitor program also provided support for this research.

APPENDIX

The m–D and v_t–D Relationships Used in Figs. 3, 4, and 5

The m–D and v_t–D relationships used to compare to ISHMAEL ice property evolution assume ice particles have sectorlike branches [m–D coefficients listed in Mitchell (1996)]. These m–D coefficients change when the diameter reaches 40 μm, and we therefore change the coefficients when the mass-weighted diameter of the distribution reaches this threshold. When the mass-weighted diameter of the distribution is less than 40 μm, ice is assumed to fall as unrimed side planes [fall speed from Locatelli and Hobbs (1974)], and otherwise ice is assumed to fall as unrimed plane dendrites [fall speed from Mitchell (1996)]. When the mass-weighted diameter of ice becomes larger than 500 μm, and if the riming rate is greater than the vapor growth rate, then ice becomes lump graupel [m–D coefficients listed in Mitchell (1996) and fall speed from Locatelli and Hobbs (1974)].

REFERENCES

Adams-Selin, R. D., S. C. van den Heever, and R. H. Johnson, 2013: Impact of graupel parameterization schemes on idealized bow echo simulations. *Mon. Wea. Rev.*, **141**, 1241–1262, doi:10.1175/MWR-D-12-00064.1.

Avramov, A., and J. Y. Harrington, 2010: Influence of parameterized ice habit on simulated mixed phase Arctic clouds. *J. Geophys. Res.*, **115**, D03205, doi:10.1029/2009JD012108.

Bailey, M. P., and J. Hallett, 2009: A comprehensive habit diagram for atmospheric ice crystals: Confirmation from the laboratory, AIRS II, and other field studies. *J. Atmos. Sci.*, **66**, 2888–2899, doi:10.1175/2009JAS2883.1.

Beheng, K., 1994: A parameterization of warm cloud microphysical conversion processes. *Atmos. Res.*, **33**, 193–206, doi:10.1016/0169-8095(94)90020-5.

Bigg, E. K., 1953: The formation of atmospheric ice crystals by the freezing of droplets. *Quart. J. Roy. Meteor. Soc.*, **79**, 510–519, doi:10.1002/qj.49707934207.

Böhm, J., 1989: A general equation for the terminal fall speed of solid hydrometeors. *J. Atmos. Sci.*, **46**, 2419–2427, doi:10.1175/1520-0469(1989)046<2419:AGEFTT>2.0.CO;2.

Chagnon, C. W., and C. E. Junge, 1961: The vertical distribution of sub-micron particles in the stratosphere. *J. Meteor.*, **18**, 746–752, doi:10.1175/1520-0469(1961)018⟨0746:TVDOSM⟩2.0.CO;2.

Chen, J.-P., and D. Lamb, 1994: The theoretical basis for the parameterization of ice crystal habits: Growth by vapor deposition. *J. Atmos. Sci.*, **51**, 1206–1221, doi:10.1175/1520-0469(1994)051<1206:TTBFTP>2.0.CO;2.

——, and ——, 1999: Simulation of cloud microphysical and chemical processes using a multicomponent framework. Part II: Microphysical evolution of a wintertime orographic cloud. *J. Atmos. Sci.*, **56**, 2293–2312, doi:10.1175/1520-0469(1999)056<2293:SOCMAC>2.0.CO;2.

——, and T.-C. Tsai, 2016: Triple-moment modal parameterization for the adaptive growth habit of pristine ice crystals. *J. Atmos. Sci.*, **73**, 2105–2122, doi:10.1175/JAS-D-15-0220.1.

Colle, B. A., M. F. Garvert, J. B. Wolfe, C. F. Mass, and C. P. Woods, 2005: The 13–14 December 2001 IMPROVE-2 event. Part III: Simulated microphysical budgets and sensitivity studies. *J. Atmos. Sci.*, **62**, 3535–3558, doi:10.1175/JAS3552.1.

DeMott, P. J., and Coauthors, 2010: Predicting global atmospheric ice nuclei distributions and their impacts on climate. *Proc.*

Natl. Acad. Sci. USA, **107**, 11 217–11 222, doi:10.1073/pnas.0910818107.

Erfani, E., and D. L. Mitchell, 2017: Growth of ice particle mass and projected area during riming. *Atmos. Chem. Phys.*, **17**, 1241–1257, doi:10.5194/acp-17-1241-2017.

Ferrier, B. S., 1994: A double-moment multiple-phase four-class bulk ice scheme. Part I: Description. *J. Atmos. Sci.*, **51**, 249–280, doi:10.1175/1520-0469(1994)051<0249:ADMMPF>2.0.CO;2.

Fovell, R. G., and Y. Ogura, 1988: Numerical simulation of a midlatitude squall line in two dimensions. *J. Atmos. Sci.*, **45**, 3846–3879, doi:10.1175/1520-0469(1988)045<3846:NSOAMS>2.0.CO;2.

Frisch, S., M. Shupe, I. Djalalova, G. Feingold, and M. Poellot, 2002: The retrieval of stratus cloud droplet effective radius with cloud radars. *J. Atmos. Oceanic Technol.*, **19**, 835–842, doi:10.1175/1520-0426(2002)019<0835:TROSCD>2.0.CO;2.

Fujiyoshi, Y., 1986: Melting snowflakes. *J. Atmos. Sci.*, **43**, 307–311, doi:10.1175/1520-0469(1986)043<0307:MS>2.0.CO;2.

Fukuta, N., and T. Takahashi, 1999: The growth of atmospheric ice crystals: A summary of findings in vertical supercooled cloud tunnel studies. *J. Atmos. Sci.*, **56**, 1963–1979, doi:10.1175/1520-0469(1999)056<1963:TGOAIC>2.0.CO;2.

Garvert, M. F., C. P. Woods, B. A. Colle, C. F. Mass, P. V. Hobbs, M. T. Stoelinga, and J. B. Wolfe, 2005: The 13–14 December 2001 IMPROVE-2 event. Part II: Comparisons of MM5 model simulations of clouds and precipitation with observations. *J. Atmos. Sci.*, **62**, 3520–3534, doi:10.1175/JAS3551.1.

Hallett, J., 1965: Field and laboratory observations of ice crystal growth from the vapor. *J. Atmos. Sci.*, **22**, 64–69, doi:10.1175/1520-0469(1965)022<0064:FALOOI>2.0.CO;2.

——, and S. C. Mossop, 1974: Production of secondary ice particles during the riming process. *Nature*, **249**, 26–28, doi:10.1038/249026a0.

Harrington, J. Y., M. P. Meyers, R. L. Walko, and W. R. Cotton, 1995: Parameterization of ice crystal conversion processes due to vapor deposition for mesoscale models using double-moment basis functions. Part I: Basic formulation and parcel model results. *J. Atmos. Sci.*, **52**, 4344–4366, doi:10.1175/1520-0469(1995)052<4344:POICCP>2.0.CO;2.

——, K. Sulia, and H. Morrison, 2013a: A method for adaptive habit prediction in bulk microphysical models. Part I: Theoretical development. *J. Atmos. Sci.*, **70**, 349–364, doi:10.1175/JAS-D-12-040.1.

——, ——, and ——, 2013b: A method for adaptive habit prediction in bulk microphysical models. Part II: Parcel model corroboration. *J. Atmos. Sci.*, **70**, 365–376, doi:10.1175/JAS-D-12-0152.1.

Hashino, T., and G. J. Tripoli, 2007: The Spectral Ice Habit Prediction System (SHIPS). Part I: Model description and simulation of the vapor deposition process. *J. Atmos. Sci.*, **64**, 2210–2237, doi:10.1175/JAS3963.1.

Heymsfield, A. J., 1977: The characteristics of graupel particles in northeastern Colorado cumulus congestus clouds. *J. Atmos. Sci.*, **35**, 284–295, doi:10.1175/1520-0469(1978)035<0284:TCOGPI>2.0.CO;2.

——, 1982: A comparative study of the rates of development of potential graupel and hail embryos in high plains storms. *J. Atmos. Sci.*, **39**, 2867–2897, doi:10.1175/1520-0469(1982)039<2867:ACSOTR>2.0.CO;2.

Jensen, A. A., and J. Y. Harrington, 2015: Modeling ice crystal aspect ratio evolution during riming: A single-particle growth model. *J. Atmos. Sci.*, **72**, 2569–2590, doi:10.1175/JAS-D-14-0297.1.

Kajikawa, M., 1972: Measurement of falling velocity of individual snow crystals. *J. Meteor. Soc. Japan*, **50**, 577–584.

Khairoutdinov, M., and Y. Kogan, 2000: A new cloud physics parameterization in a large-eddy simulation model of marine stratocumulus. *Mon. Wea. Rev.*, **128**, 229–243, doi:10.1175/1520-0493(2000)128<0229:ANCPPI>2.0.CO;2.

Kintea, D. M., T. Hauk, I. V. Roisman, and C. Tropea, 2015: Shape evolution of a melting nonspherical particle. *Phys. Rev.*, **92E**, 033012, doi:10.1103/PhysRevE.92.033012.

Knight, C. A., 1979: Observations of the morphology of melting snow. *J. Atmos. Sci.*, **36**, 1123–1130, doi:10.1175/1520-0469(1979)036<1123:OOTMOM>2.0.CO;2.

Kong, F., and M. Yau, 1997: An explicit approach to microphysics in MC2. *Atmos.–Ocean*, **35**, 257–291, doi:10.1080/07055900.1997.9649594.

Lamb, D., and W. Scott, 1972: Linear growth rates of ice crystals grown from the vapor phase. *J. Cryst. Growth*, **12**, 21–31, doi:10.1016/0022-0248(72)90333-8.

——, and J. Verlinde, 2011: *Physics and Chemistry of Clouds*. Cambridge University Press, 600 pp.

Libbrecht, K., 2003: Growth rates of the principal facets of ice between −10°C and −40°C. *J. Cryst. Growth*, **247**, 530–540, doi:10.1016/S0022-0248(02)01996-6.

Lin, Y., and B. A. Colle, 2009: The 4–5 December 2001 IMPROVE-2 event: Observed microphysics and comparisons with the weather research and forecasting model. *Mon. Wea. Rev.*, **137**, 1372–1392, doi:10.1175/2008MWR2653.1.

——, and ——, 2011: A new bulk microphysical scheme that includes riming intensity and temperature-dependent ice characteristics. *Mon. Wea. Rev.*, **139**, 1013–1035, doi:10.1175/2010MWR3293.1.

Locatelli, J. D., and P. V. Hobbs, 1974: Fall speeds and masses of solid precipitation particles. *J. Geophys. Res.*, **79**, 2185–2197, doi:10.1029/JC079i015p02185.

Macklin, W. C., 1962: The density and structure of ice formed by accretion. *Quart. J. Roy. Meteor. Soc.*, **88**, 30–50, doi:10.1002/qj.49708837504.

Magono, C., and C. W. Lee, 1966: Meteorological classification of natural snow crystals. *J. Fac. Sci. Hokkaido Univ. Ser. 7*, **2**, 321–335.

Mansell, E. R., C. L. Ziegler, and E. C. Bruning, 2010: Simulated electrification of a small thunderstorm with two-moment bulk microphysics. *J. Atmos. Sci.*, **67**, 171–194, doi:10.1175/2009JAS2965.1.

Marshall, J. S., and W. M. K. Palmer, 1948: The distribution of raindrops with size. *J. Meteor.*, **5**, 165–166, doi:10.1175/1520-0469(1948)005<0165:TDORWS>2.0.CO;2.

Mason, B. J., 1953: The growth of ice crystals in a supercooled water cloud. *Quart. J. Roy. Meteor. Soc.*, **79**, 104–111, doi:10.1002/qj.49707933909.

Meyers, M. P., R. L. Walko, J. Y. Harrington, and W. R. Cotton, 1997: New RAMS cloud microphysics parameterization. Part II: The two-moment scheme. *Atmos. Res.*, **45**, 3–39, doi:10.1016/S0169-8095(97)00018-5.

Milbrandt, J. A., and M. K. Yau, 2005a: A multimoment bulk microphysics parameterization. Part I: Analysis of the role of the spectral shape parameter. *J. Atmos. Sci.*, **62**, 3051–3064, doi:10.1175/JAS3534.1.

——, and ——, 2005b: A multimoment bulk microphysics parameterization. Part II: A proposed three-moment closure and scheme description. *J. Atmos. Sci.*, **62**, 3065–3081, doi:10.1175/JAS3535.1.

——, and H. Morrison, 2013: Prediction of graupel density in a bulk microphysics scheme. *J. Atmos. Sci.*, **70**, 410–429, doi:10.1175/JAS-D-12-0204.1.

——, and ——, 2016: Parameterization of cloud microphysics based on the prediction of bulk ice particle properties. Part III: Introduction of multiple free categories. *J. Atmos. Sci.*, **73**, 975–995, doi:10.1175/JAS-D-15-0204.1.

Miles, N. L., J. Verlinde, and E. E. Clothiaux, 2000: Cloud droplet size distributions in low-level stratiform clouds. *J. Atmos. Sci.*, **57**, 295–311, doi:10.1175/1520-0469(2000)057<0295:CDSDIL>2.0.CO;2.

Minder, J. R., and D. E. Kingsmill, 2013: Mesoscale variations of the atmospheric snow line over the northern Sierra Nevada: Multiyear statistics, case study, and mechanisms. *J. Atmos. Sci.*, **70**, 916–938, doi:10.1175/JAS-D-12-0194.1.

Mitchell, D. L., 1996: Use of mass- and area-dimensional power laws for determining precipitation particle terminal velocities. *J. Atmos. Sci.*, **53**, 1710–1723, doi:10.1175/1520-0469(1996)053<1710:UOMAAD>2.0.CO;2.

——, and A. J. Heymsfield, 2005: Refinements in the treatment of ice particle terminal velocities, highlighting aggregates. *J. Atmos. Sci.*, **62**, 1637–1644, doi:10.1175/JAS3413.1.

Mitra, S. K., O. Vohl, M. Ahr, and H. R. Pruppacher, 1990: A wind tunnel and theoretical study of the melting behavior of atmospheric ice particles. IV: Experiment and theory for snow flakes. *J. Atmos. Sci.*, **47**, 584–591, doi:10.1175/1520-0469(1990)047<0584:AWTATS>2.0.CO;2.

Morrison, H., and W. W. Grabowski, 2008: A novel approach for representing ice microphysics in models: Description and tests using a kinematic framework. *J. Atmos. Sci.*, **65**, 1528–1548, doi:10.1175/2007JAS2491.1.

——, and J. A. Milbrandt, 2015: Parameterization of cloud microphysics based on the prediction of bulk ice particle properties. Part I: Scheme description and idealized tests. *J. Atmos. Sci.*, **72**, 287–311, doi:10.1175/JAS-D-14-0065.1.

——, ——, G. H. Bryan, K. Ikeda, S. A. Tessendorf, and G. Thompson, 2015: Parameterization of cloud microphysics based on the prediction of bulk ice particle properties. Part II: Case study comparisons with observations and other schemes. *J. Atmos. Sci.*, **72**, 312–339, doi:10.1175/JAS-D-14-0066.1.

——, A. A. Jensen, J. Y. Harrington, and J. A. Milbrandt, 2016: Advection of coupled hydrometeor quantities in bulk cloud microphysics schemes. *Mon. Wea. Rev.*, **144**, 2809–2829, doi:10.1175/MWR-D-15-0368.1.

Murakami, M., 1990: Numerical modeling of dynamical and microphysical evolution of an isolated convective cloud. *J. Meteor. Soc. Japan*, **68**, 107–128, doi:10.2151/jmsj1965.68.2_107.

Ono, A., 1970: Growth mode of ice crystals in natural clouds. *J. Atmos. Sci.*, **27**, 649–658, doi:10.1175/1520-0469(1970)027<0649:GMOICI>2.0.CO;2.

Rutledge, S. A., and P. V. Hobbs, 1983: The mesoscale and microscale structure and organization of clouds and precipitation in midlatitude cyclones. VIII: A model for the "seeder-feeder" process in warm-frontal rainbands. *J. Atmos. Sci.*, **40**, 1185–1206, doi:10.1175/1520-0469(1983)040<1185:TMAMSA>2.0.CO;2.

Sheridan, L. M., 2008: Deposition coefficient, habit and ventilation influences on cirriform cloud properties. M.S. thesis, Dept. of Meteorology and Atmospheric Science, The Pennsylvania State University, 102 pp. [Available online at https://etda.libraries.psu.edu/catalog/8556.]

Smolarkiewicz, P. K., 1984: A fully multidimensional positive definite advection transport algorithm with small implicit diffusion. *J. Comput. Phys.*, **54**, 325–362, doi:10.1016/0021-9991(84)90121-9.

——, and L. G. Margolin, 1998: MPDATA: A finite-difference solver for geophysical flows. *J. Comput. Phys.*, **140**, 459–480, doi:10.1006/jcph.1998.5901.

Straka, J. M., and E. R. Mansell, 2005: A bulk microphysics parameterization with multiple ice precipitation categories. *J. Appl. Meteor.*, **44**, 445–466, doi:10.1175/JAM2211.1.

Sulia, K. J., and J. Y. Harrington, 2011: Ice aspect ratio influences on mixed-phase clouds: Impacts on phase partitioning in parcel models. *J. Geophys. Res.*, **116**, D21309, doi:10.1029/2011JD016298.

——, ——, and H. Morrison, 2013: A method for adaptive habit prediction in bulk microphysical models. Part III: Applications and studies within a two-dimensional kinematic model. *J. Atmos. Sci.*, **70**, 3302–3320, doi:10.1175/JAS-D-12-0316.1.

——, H. Morrison, and J. Y. Harrington, 2014: Dynamical and microphysical evolution during mixed-phase cloud glaciation simulated using the bulk adaptive habit prediction model. *J. Atmos. Sci.*, **71**, 4158–4180, doi:10.1175/JAS-D-14-0070.1.

Szeto, K. K., and H.-R. Cho, 1994: A numerical investigation of squall lines. Part III: Sensitivity to precipitation processes and the Coriolis force. *J. Atmos. Sci.*, **51**, 1341–1351, doi:10.1175/1520-0469(1994)051<1341:ANIOSL>2.0.CO;2.

Szumowski, M. J., W. W. Grabowski, and H. T. Ochs III, 1998: Simple two-dimensional kinematic framework designed to test warm rain microphysical models. *Atmos. Res.*, **45**, 299–326, doi:10.1016/S0169-8095(97)00082-3.

Takahashi, T., and N. Fukuta, 1988: Supercooled cloud tunnel studies on the growth of snow crystals between −4 and −20°C. *J. Meteor. Soc. Japan*, **66**, 841–855, doi:10.2151/jmsj1965.66.6_841.

——, T. Endoh, and G. Wakahama, 1991: Vapor diffusional growth of free-falling snow crystals between −3 and −23°C. *J. Meteor. Soc. Japan*, **69**, 15–30.

Thompson, G., P. R. Field, R. M. Rasmussen, and W. D. Hall, 2008: Explicit forecasts of winter precipitation using an improved bulk microphysics scheme. Part II: Implementation of a new snow parameterization. *Mon. Wea. Rev.*, **136**, 5095–5115, doi:10.1175/2008MWR2387.1.

Verlinde, J., and W. R. Cotton, 1993: Fitting microphysical observations of nonsteady convective clouds to a numerical model: An application of the adjoint technique of data assimilation to a kinematic model. *Mon. Wea. Rev.*, **121**, 2776–2793, doi:10.1175/1520-0493(1993)121<2776:FMOONC>2.0.CO;2.

Walko, R., W. Cotton, M. Meyers, and J. Harrington, 1995: New RAMS cloud microphysics parameterization part I: The single-moment scheme. *Atmos. Res.*, **38**, 29–62, doi:10.1016/0169-8095(94)00087-T.

Wang, P. K., and W. Ji, 2000: Collision efficiencies of ice crystals at low–intermediate Reynolds numbers colliding with supercooled cloud droplets: A numerical study. *J. Atmos. Sci.*, **57**, 1001–1009, doi:10.1175/1520-0469(2000)057<1001:CEOICA>2.0.CO;2.

Wisner, C., H. D. Orville, and C. Myers, 1972: A numerical model of a hail-bearing cloud. *J. Atmos. Sci.*, **29**, 1160–1181, doi:10.1175/1520-0469(1972)029<1160:ANMOAH>2.0.CO;2.

Woods, C. P., M. T. Stoelinga, and J. D. Locatelli, 2007: The IMPROVE-1 storm of 1–2 February 2001. Part III: Sensitivity of a mesoscale model simulation to the representation of snow particle types and testing of a bulk microphysical scheme with snow habit prediction. *J. Atmos. Sci.*, **64**, 3927–3948, doi:10.1175/2007JAS2239.1.